

Suppression exponent for multiparticle production in $\lambda\phi^4$ theory

S.V. Demidov^{a,b} B.R. Farkhtdinov^{a,b,c} D.G. Levkov^{a,d}

^a*Institute for Nuclear Research of the Russian Academy of Sciences, Moscow 117312, Russia*

^b*Moscow Institute of Physics and Technology, Dolgoprudny 141700, Russia*

^c*I.M. Sechenov First Moscow State Medical University, Moscow 119991, Russia*

^d*Institute for Theoretical and Mathematical Physics, MSU, Moscow 119991, Russia*

ABSTRACT: We compute the probability of producing n particles from few colliding particles in the unbroken $(3 + 1)$ -dimensional $\lambda\phi^4$ theory. To this end we numerically implement semiclassical method of singular solutions which works at $n \gg 1$ in the weakly coupled regime $\lambda \ll 1$. For the first time, we obtain reliable results in the region of exceptionally large final-state multiplicities $n \gg \lambda^{-1}$ where the probability decreases exponentially with n , $\mathcal{P}(\text{few} \rightarrow n) \sim \exp\{f_\infty(\varepsilon)n\}$, and its slope $f_\infty < 0$ depends on the mean kinetic energy ε of produced particles. In the opposite case $n \ll \lambda^{-1}$ our data match well-known tree-level result, and they interpolate between the two limits at $n \sim \lambda^{-1}$. Overall, this proves exponential suppression of the multiparticle production probability at $n \gg 1$ and arbitrary ε in the unbroken theory. Using numerical solutions, we critically analyze the mechanism for multiple Higgs boson production suggested in the literature. Application of our technique to the scalar theory with spontaneously broken symmetry can eradicate (or confirm) it in the nearest future.

In memory of Valery Rubakov

Contents

1	Introduction and main results	1
2	Semiclassical method	7
2.1	Saddle-point equations	7
2.2	Numerical implementation	9
3	A way to singular solutions	11
4	Numerical results	14
4.1	Semiclassical solutions	14
4.2	Suppression exponent	18
5	Discussion	21
A	Lattice formulation	26
B	Solutions in the linear theory	30
C	Singularity structure and the limit $J \rightarrow 0$	30

1 Introduction and main results

Perturbative method is efficient for computing few-to-few scattering amplitudes in weakly coupled field theories. But it may become unreliable [1–4] if the number n of particles in the final state exceeds the inverse coupling constant λ^{-1} of the theory. Indeed, the count of tree diagrams contributing to $\text{few} \rightarrow n$ processes in models of scalar fields grows factorially [3–5] with n , and l -loop corrections add even more — of order $n!n^{l+1}$ — terms, see [6–8] and Figs. 1a,b. As a consequence, perturbative series for the respective amplitudes are proportional to $n!$, go in powers of λn instead of λ , and explode at $n \gtrsim \lambda^{-1}$ [8–10]. This simplified bookkeeping is supported by explicit calculations in the scalar field theories at tree [5, 11–14] and one-loop [6, 7, 15, 16] levels, both at the mass threshold of n final particles and for their nonzero spatial momenta [8, 17, 18]. It also agrees with the intuition acquired from one-dimensional quantum mechanics [19–21].

Later, it was observed [8] that the parts of perturbative series going in powers of λn can be resummed into an exponent of a universal “holy grail” function F . Consider, say, the scalar $\lambda\phi^4$ theory and inclusive probability $\mathcal{P}_n(E)$ of producing n scalar quanta with total

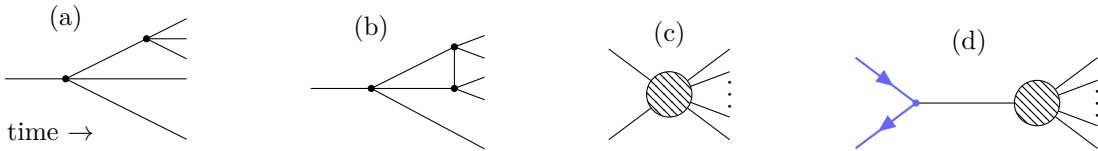


Figure 1: Examples of (a) tree and (b) one-loop diagrams describing creation of $n = 5$ bosons from one off-shell particle in the scalar $\lambda\phi^4$ theory. The numbers of such graphs grow with the final-state multiplicity as $\sim n!$ and $\sim n^2 n!$, respectively. (c), (d) Processes $\text{few} \rightarrow n$ for different operators \hat{O} in Eq. (1.1).

energy E from the few-particle initial state $\hat{O}|0\rangle$. At $n \sim \lambda^{-1} \gg 1$ this probability is expected to have the form [8],

$$\mathcal{P}_n(E) \equiv \sum_f |\langle f; E, n | \hat{S} \hat{O} | 0 \rangle|^2 \sim e^{F(\lambda n, \varepsilon)/\lambda}, \quad (1.1)$$

where the sum covers all final states with given n and E , \hat{S} is the S-matrix, and the exponent in the right-hand side collects all leading terms of the perturbative series at fixed λn . The initial state operator \hat{O} may create two ϕ -quanta — then \mathcal{P}_n is proportional to the familiar $2 \rightarrow n$ cross section (Fig. 1c). Otherwise, one can take $\hat{O} \propto \hat{\phi}(0)$ if the off-shell ϕ -boson is initially produced in an external collision, see Fig. 1d. In any case, the exponent F is conjectured to be *universal* [22], i.e. independent of the operator \hat{O} as long as the latter creates $\ll \lambda^{-1}$ particles from the vacuum. This makes F a function of two variables: the combination $\lambda n \sim O(1)$ and mean kinetic energy $\varepsilon \equiv E/n - m$ of final particles with mass m .

To date, the form (1.1) of the probability and universality of the exponent are confirmed in the $\lambda\phi^4$ theory [8, 22] for the two leading terms of F expansion in λn , for many expansion orders in the analogous quantum mechanics [20, 21], and for the sister processes of underbarrier tunneling between the few-particle and multiparticle states¹ [24–27]. All these tests are nonperturbative because the right-hand side of Eq. (1.1) includes arbitrarily high powers of λ even in the simplest case when F is cropped to $O(\lambda n)$ and $O(\lambda n)^2$ terms. At the same time, no reliable first-principle calculation of the exponent has yet been performed at $n \sim \lambda^{-1}$ in any field theoretical model, see Refs. [28–37] for similar results in the case of tunneling.

Expression (1.1) reveals exponential sensitivity of the scattering probability to the number of particles in the final state. One asks [1, 2] whether it may become unsuppressed at sufficiently large $n \sim \lambda^{-1}$. Recently, this question was acutely posed in the context of the so-called “Higgspllosion” scenario [38–40]: the exponent for producing n nonrelativistic Higgs bosons from two colliding gluons was suggested to have the form,

$$F_{\text{Higgspllosion}} \approx \lambda n \ln \frac{\lambda n}{4} + \frac{3}{2} \lambda n \ln \frac{\varepsilon}{3\pi m} + \frac{\lambda n}{2} + 0.854 (\lambda n)^{3/2} \quad \text{at } n \leq n_*. \quad (1.2)$$

¹In the latter case universality of the exponent is called Rubakov-Son-Tinyakov conjecture [23].

Here m , λ , and $\varepsilon \ll m$ are the mass, quartic constant, and mean kinetic energy of the final-state Higgs bosons, $E = n(m+\varepsilon)$ is the collision energy, and n_* is defined by $F_{\text{Higgspllosion}}(\lambda n_*) = 0$. Importantly, Eq. (1.2) was derived semiclassically at $n \sim \lambda^{-1}$, albeit with daring assumptions on the structure of semiclassical solutions [39, 40]. It may well be valid in the entire region of multiplicities $n \leq n_* \sim 3.08 \lambda^{-1} \ln^2(\varepsilon/m)$ where the exponent is non-positive — then the transitions become unsuppressed at $n \approx n_*$. At larger n corrections to Eq. (1.2) should prevail [38, 41] and unitarize the theory because the probability \mathcal{P}_n cannot be exponentially large², cf. [44–46]. But even in its limited parameter space Eq. (1.2) can drastically change the entire Higgs phenomenology predicting explosive production of these particles in high-energy collisions and in decays of new heavy resonances [38, 47], cf. [48].

On the other hand, one finds this outstanding possibility challenging from the consistency side of quantum theory. Indeed, recall that the inclusive probability of high-energy scattering is related — by optical theorem and dispersion relations — to the Green’s function of few field operators at low momenta. If the transitions from “few” to “many” were unsuppressed at high energies, the Green’s functions would receive sizeable contributions from virtual multiparticle states, and that would break perturbative expansion at small momenta [9, 44]. This argument may be brushed off as inconclusive [43], but it certainly raises the stakes: either Eq. (1.2) is invalid or one of the building blocks of a consistent quantum field theory — dispersion relations or the perturbative method — should be abandoned. We will return to this issue in the Discussion section.

Another warning comes from simulations of classical waves. If the probability of multiparticle production were of order one, the time-reversed processes, namely, conversion of many particles into few highly energetic quanta would also proceed classically [49–51]. The latter conversion was not, however, observed in evolutions of classical wave packets — read, collisions of multiparticle states — despite Monte Carlo optimization over the available parameter space [52]. A possible loophole here is a different model: unbroken $\lambda\phi^4$ theory in Ref. [52] as compared to the spontaneously broken case used for deriving Eq. (1.2).

In this paper we numerically compute the exponent $F(\lambda n, \varepsilon)$ at arbitrary λn from first principles in the scalar field theory. Up to our knowledge, no calculation of this kind was performed before, see Ref. [53] for the accompanying work. We exploit the same semiclassical method [54] as in the studies on “Higgspllosion” [39, 40], but do not make additional assumptions on the structure of saddle-point solutions. We consider $(3+1)$ -dimensional $\lambda\phi^4$ theory with positive mass term $m^2 > 0$ and no spontaneous symmetry breaking:

$$S = \frac{1}{2\lambda} \int d^4x \left(-\phi \square \phi - m^2 \phi^2 - \phi^4/2 \right), \quad (1.3)$$

where the coupling $\lambda \ll 1$ appears in front of the action and hence governs loop expansion; one can bring it in front of the ϕ^4 term using the field redefinition $\phi \rightarrow \phi\sqrt{\lambda}$.

We rely on the semiclassical technique of D.T. Son [54] developed as an adaptation of L.D. Landau method for calculating matrix elements in quantum mechanics [55]; see also [56–

²Also, large- n asymptotic of Eq. (1.2) is inconsistent with locality of quantum theory [42, 43].

59]. It applies at $n \gg 1$ and $\lambda \ll 1$ and is based on the universality of the exponent in Eq. (1.1). Namely, since F is independent of the few-particle operator \hat{O} , we can take it in the form

$$\hat{O} = \exp \left\{ -\frac{1}{\lambda} \int d^3 \mathbf{x} J(\mathbf{x}) \hat{\phi}(0, \mathbf{x}) \right\} \quad (1.4)$$

that describes a classical source $J(\mathbf{x})$ acting at $t = 0$. The latter source creates $O(J^2/\lambda)$ particles from the vacuum, i.e. a few-particle initial state with multiplicity $\ll \lambda^{-1}$ at $J \ll O(\lambda^0)$. Then the universality conjecture guarantees that the limit

$$F(\lambda n, \varepsilon) = \lim_{J \rightarrow 0} F_J(\lambda n, \varepsilon) \quad (1.5)$$

exists and is independent of the source profile, where F_J in the right-hand side is computed at nonzero $J(\mathbf{x})$.

The above observation opens up a way to the semiclassical description because at $O(J^2/\lambda) \gg 1$ and $n \gg 1$ both the initial and final states of the process include many particles. Therefore, one can compute F_J semiclassically and then take the limit $J \rightarrow 0$, thus arriving at the exponent of the few $\rightarrow n$ production probability. We stress that the last limit brings the initial multiplicity to the region $1 \ll O(J^2/\lambda) \ll \lambda^{-1}$ where the exponent is already universal but the semiclassical method is still applicable.

At finite J , the standard semiclassical machinery [23, 54, 60] works in the following way. One writes the probability (1.1) in the form of a path integral and evaluates the latter in the saddle-point approximation. The respective saddle-point configurations $\phi_{\text{cl}}(t, \mathbf{x})$ are generically complex. They satisfy the classical field equation in the presence of an external source $J(\mathbf{x})$ and the boundary conditions at $t \rightarrow \pm\infty$ depending on ε and λn . Once the semiclassical solutions are found, F_J can be computed using the value of the action functional on $\phi_{\text{cl}}(t, \mathbf{x})$. Notably, the semiclassical configurations become singular in the limit $J \rightarrow 0$; that is why the overall technique is called the method of singular solutions [54]. Previously, it was shown [9, 54] that this method correctly reproduces tree-level and one-loop multiparticle amplitudes at the threshold ($\varepsilon = 0$) in the $\lambda\phi^4$ theory. Besides, in Ref. [61] it was used to calculate tree-level suppression exponent at $\lambda n \ll 1$ and arbitrary ε . But apart from the controversial ‘‘Higgspllosion’’ studies, the most interesting case $n \gtrsim \lambda^{-1}$ was never considered.

In this paper we numerically find the saddle-point solutions $\phi_{\text{cl}}(t, \mathbf{x})$ at arbitrary λn and ε in the model (1.3). We make no assumptions on their properties or analytic structure. We reliably select physically relevant configurations that give dominant contributions to the probability. Namely, at certain nonzero J the out-particles are mainly produced by the classical source itself, while the interaction of the scalar field can be ignored. In this case the physical solutions can be found in the free theory with a source. Switching on interaction and gradually decreasing J to zero at fixed λn and ε , we arrive at a continuous branch of relevant saddle-point configurations. The subsequent extrapolation $J \rightarrow 0$ gives the sought-for singular solutions and their suppression exponent F in the broad range of $n \gg 1$ and ε .

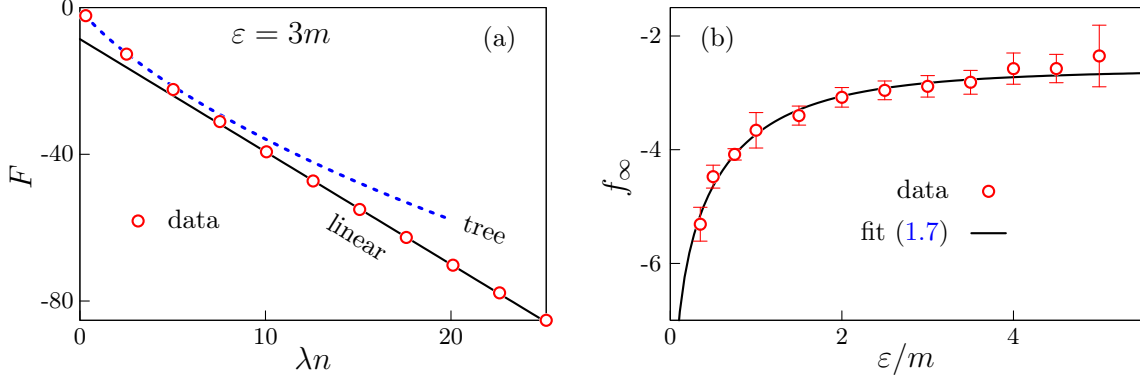


Figure 2: (a) The exponent $F(\lambda n, \varepsilon)$ of the multiparticle production probability in the model (1.3) at $\varepsilon = 3m$. Numerical data (circles) interpolate between the tree-level result at $\lambda n \ll 1$ (dashed line and Eq. (4.4) from the main text) and linear asymptotic (1.6) at $\lambda n \gg 1$ (solid line). (b) The slope $f_\infty(\varepsilon)$ of the exponent at large λn as a function of ε .

Our result for the exponent $F(\lambda n, \varepsilon)$ is demonstrated in Fig. 2a (circles) at the exemplary value $\varepsilon = 3m$ with numerical accuracy better than the circle size. We see that F monotonically decreases with λn . As expected, at $\lambda n \ll 1$ it coincides with the contribution of tree-level diagrams [62] (dashed line), see also [53]. In the opposite limit $\lambda n \gg 1$ our numerical data are well fitted by the linear function (solid line in the figure):

$$F \rightarrow \lambda n f_\infty(\varepsilon) + g_\infty(\varepsilon) \quad \text{or} \quad \mathcal{P}_n \rightarrow e^{n f_\infty(\varepsilon) + g_\infty(\varepsilon)/\lambda} \quad \text{at} \quad \lambda n \rightarrow +\infty, \quad (1.6)$$

where f_∞ and g_∞ are negative. In the main text we will show that results at other ε have similar qualitative behavior, although f_∞ and g_∞ depend on ε . In particular, Fig. 2b demonstrates the slope $f_\infty(\varepsilon) < 0$ increasing with energy. It can be approximated by the expression (solid line in the figure)

$$f_\infty(\varepsilon) \approx -\frac{3}{4} \ln [(d_1 m/\varepsilon)^2 + d_2], \quad d_i \approx \{10.7, 30.7\} \quad (1.7)$$

that has physically motivated asymptotics at $\varepsilon \rightarrow 0, +\infty$; see the main text for derivation. Minimal slope $f_\infty \rightarrow -2.57 \pm 0.06$ is achieved in the ultrarelativistic limit $\varepsilon \rightarrow +\infty$.

It is remarkable that the probability (1.1) can be used to calculate the amplitude \mathcal{A}_n of producing n particles at the mass threshold. Indeed, in the limit $\varepsilon \rightarrow 0$ a single out-state remains: the one with zero spatial momenta of all final particles. The amplitude of transition to this state is determined by the ratio of the inclusive probability to the n -particle phase volume $\mathcal{V}_n(\varepsilon)/n!$ at $\varepsilon \rightarrow 0$:

$$|\mathcal{A}_n|^2 \sim \lim_{\varepsilon \rightarrow 0} \frac{n!}{\mathcal{V}_n} e^{F/\lambda} \sim n! m^{4-2n} e^{2F_{\mathcal{A}}(\lambda n)/\lambda}, \quad (1.8)$$

where the factor $n!$ explicitly accounts for particle identity, the standard expression for \mathcal{V}_n is given in the main text, and the last equality fixes the expected parametric form of the

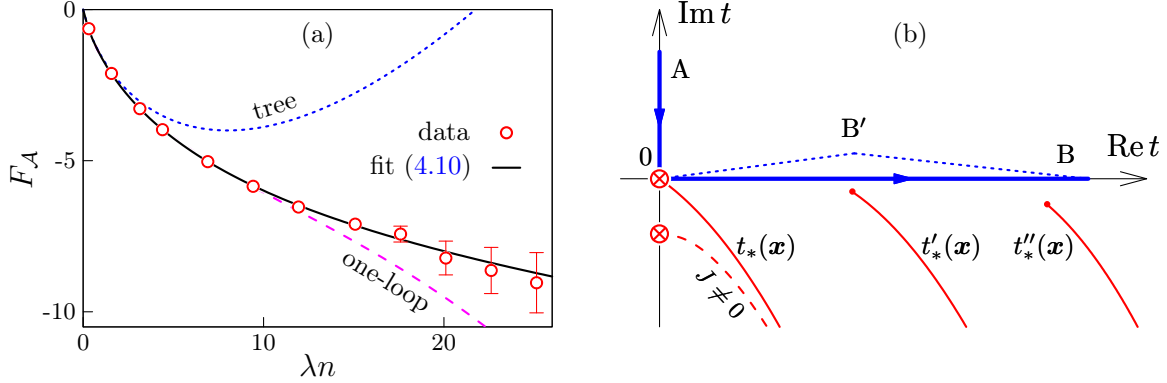


Figure 3: (a) Suppression exponent $F_A(\lambda n)$ of the amplitude to produce n particles at the mass threshold, see Eq. (1.8). (b) Complex time contour A0B for the semiclassical boundary value problem (thick solid line) and the singularities $t_*(\mathbf{x})$, $t'_*(\mathbf{x})$, $t''_*(\mathbf{x})$ of the semiclassical solutions (thin lines starting from crossed circles or filled points); not to scale.

amplitude at $n \sim \lambda^{-1}$. Extrapolating numerical results to $\varepsilon = 0$, we get the exponent $F_A(\lambda n)$ which is displayed by circles with errorbars in Fig. 3a. At small λn these data are close to the tree-level exponent of Ref. [5] (dotted line) and even closer to the one-loop result of Refs. [6, 8] (dashed line). At large λn the data deviate from the perturbative results, but they are well fitted by the function with linear asymptotic as $\lambda n \rightarrow +\infty$ (solid line and Eq. (4.10) from the main text). In the latter large- λn region the amplitude equals

$$|\mathcal{A}_n| \sim m^{2-n} \sqrt{n!} e^{n f'_\infty + g'_\infty / \lambda}, \quad f'_\infty = -0.062 \pm 0.026, \quad g'_\infty = -9.7 \pm 1.2 \quad \text{at } n \gg \lambda^{-1}. \quad (1.9)$$

We will explain below that Eq. (1.9) does not contradict to unitarity of quantum theory despite the factorial dependence on n .

In a nutshell, our results prove that the probability of producing $n \gg 1$ particles from few colliding quanta is exponentially suppressed in the unbroken $\lambda\phi^4$ theory. In addition to already presented data, below we visualize the suppression exponent at different ε , fit it with a convenient formula at finite λn , and provide tabulated raw data in the ancillary files [63]. We also confirm universality of the exponent by comparing results at different source profiles $J(\mathbf{x})$. Finally, we will discuss self-consistency of Eqs. (1.6) and (1.9), physical constraints on F , and reiterate interconnections between the multiparticle probability, unitarity, perturbative series, and dispersion relations.

An important part of our study is the analysis of configurations $\phi_{c1}(t, \mathbf{x})$ saturating the probability (1.1). Although being complex and with no immediate physical meaning, they characterize the dynamics of the process and specify its most probable final state. Studying the analytic structure of the solutions, we find out that one of the assumptions underlying the ‘‘Higgspllosion’’ scenario [39, 40] is not generic. This puts Eq. (1.2) on shaky ground despite the fact that it was obtained in a different model.

The rest of this paper is organized as follows. We review the semiclassical method of singular solutions and formulate it on the lattice in Sec. 2. Section 3 explains our techniques for selecting physically relevant solutions and for extrapolating the data to $J \rightarrow 0$. We present results in Sec. 4 and discuss them in Sec. 5. Appendices A,B, and C provide details of numerical methods, saddle-point solutions in the linear theory, and analysis of singularities, respectively.

2 Semiclassical method

2.1 Saddle-point equations

We start by reviewing equations for the saddle-point configurations $\phi_{\text{cl}}(t, \mathbf{x})$ saturating path integral for the probability (1.1) at $\lambda \ll 1$ and large n , see [23, 40, 54, 60] for derivation.

Generically, ϕ_{cl} are complex and satisfy the field equation

$$\square\phi_{\text{cl}} + m^2\phi_{\text{cl}} + \phi_{\text{cl}}^3 = iJ(\mathbf{x})\delta(t), \quad (2.1)$$

where the source in the right-hand side originates from the operator $\hat{\mathcal{O}}$ in the form (1.4). Boundary conditions for this equation are related to the initial and final states of the process.

It will be convenient to analytically continue $\phi_{\text{cl}}(t, \mathbf{x})$ onto the complex time contour A0B in Fig. 3b, i.e. perform a partial Wick rotation. Then the first boundary condition requires the field to vanish in the infinite past along the Euclidean time axis:

$$\phi_{\text{cl}}(t, \mathbf{x}) \rightarrow 0 \quad \text{as} \quad t \rightarrow +i\infty. \quad (2.2)$$

This corresponds to initial vacuum in Eq. (1.1). In the infinite future $t \rightarrow +\infty$, the semiclassical solution describes a state of n free particles. Hence, it should linearize into a superposition of free waves:

$$\phi_{\text{cl}}(t, \mathbf{x}) \rightarrow \int \frac{d^3\mathbf{k}}{(2\pi)^{3/2}\sqrt{2\omega_{\mathbf{k}}}} e^{i\mathbf{k}\mathbf{x}} [a_{\mathbf{k}}e^{-i\omega_{\mathbf{k}}t} + b_{-\mathbf{k}}^*e^{i\omega_{\mathbf{k}}t}] \quad \text{as} \quad t \rightarrow +\infty, \quad (2.3)$$

where $\omega_{\mathbf{k}} \equiv \sqrt{\mathbf{k}^2 + m^2}$ and $a_{\mathbf{k}}$ and $b_{\mathbf{k}}$ are the negative- and positive-frequency amplitudes, respectively. The second boundary condition relates the amplitudes:

$$a_{\mathbf{k}} = e^{-\theta + 2\omega_{\mathbf{k}}T} b_{\mathbf{k}}. \quad (2.4)$$

One can show [23] that this equation corresponds to inclusive final state with given energy and multiplicity in Eq. (1.1). Parameters T and θ in its right-hand side are the Lagrange multipliers related to E and n via the standard expressions

$$\lambda E = \int d^3\mathbf{k} \omega_{\mathbf{k}} a_{\mathbf{k}} b_{\mathbf{k}}^*, \quad \lambda n = \int d^3\mathbf{k} a_{\mathbf{k}} b_{\mathbf{k}}^*. \quad (2.5)$$

We will also use kinetic energy per final particle $\varepsilon \equiv E/n - m$.

It is worth noting that a complete Wick rotation to the Euclidean axis cannot be performed. Indeed, $b_{\mathbf{k}}$ cannot vanish for all \mathbf{k} at nonzero E and n due to Eqs. (2.5). Thus, the positive-frequency part of the solution (2.3) grows exponentially at $t \rightarrow -i\infty$, ruins linearity and makes it impossible to impose free-wave boundary conditions in that region. On the other hand, the semiclassical equations can be consistently formulated on the contour A0B, and the source $J(\mathbf{x})\delta(t)$ can be placed right in its corner at $t = 0$. The latter fact is made explicit by integrating Eq. (2.1) across $t = 0$. We get,

$$\partial_t \phi_{\text{cl}}(+0, \mathbf{x}) - \partial_t \phi_{\text{cl}}(+i0, \mathbf{x}) = iJ(\mathbf{x}), \quad \phi_{\text{cl}}(+0, \mathbf{x}) = \phi_{\text{cl}}(+i0, \mathbf{x}) \quad \text{at } t = 0. \quad (2.6)$$

Hence, one can find the solutions of Eq. (2.1) with zero right-hand side on the parts A0 and 0B of the time contour and then glue them at $t = 0$ using Eq. (2.6).

Equations (2.1)–(2.5) form a complete boundary value problem for the semiclassical configuration $\phi_{\text{cl}}(t, \mathbf{x})$ and Lagrange multipliers T, θ . Once the equations are solved, one calculates the suppression exponent [54],

$$F_J = 2\lambda ET - \lambda n\theta - 2\lambda \text{Im} S[\phi_{\text{cl}}] - 2\text{Re} \int d^3\mathbf{x} J(\mathbf{x}) \phi_{\text{cl}}(0, \mathbf{x}), \quad (2.7)$$

where the first two terms come from the non-vacuum final state, the classical action (1.3) in the third term is evaluated on ϕ_{cl} , and the last term accounts for the insertion of the operator $\hat{\mathcal{O}}$. Note that the semiclassical equations involve λ, n , and E only in the combinations λn and λE , see Eq. (2.5). This makes the rescaled classical action $\lambda S[\phi_{\text{cl}}]$ and the semiclassical exponent F_J depend on two parameters: λn and $\varepsilon \equiv E/n - m$.

It is also worth pointing out that the Lagrange multipliers T and θ automatically satisfy Legendre transform relations [54]:

$$2T = \frac{\partial F_J}{\partial(\lambda E)}, \quad \theta = -\frac{\partial F_J}{\partial(\lambda n)}. \quad (2.8)$$

This discloses them as derivatives of the suppression exponent $F_J(\lambda n, \lambda E)$. We will use Eqs. (2.8) as a cross-check of the numerical method and a cheap way to increase precision.

The last step of the semiclassical method is to send $J \rightarrow 0$. Let us demonstrate [54] that the semiclassical solutions become singular in this limit. Consider their energy

$$\mathcal{E}(t) = \frac{1}{2\lambda} \int d^3\mathbf{x} [(\partial_t \phi_{\text{cl}})^2 + (\partial_{\mathbf{x}} \phi_{\text{cl}})^2 + m^2 \phi_{\text{cl}}^2 + \phi_{\text{cl}}^4/2], \quad (2.9)$$

which separately conserves on the Euclidean and Minkowski parts A0 and 0B of the time contour. Namely, $\mathcal{E} = 0$ on the part A0 and $\mathcal{E} = E$ on the part 0B due to boundary conditions (2.2) and (2.5). The energy jumps at $t = 0$ due to presence of the classical source J . We therefore obtain,

$$\lambda E = \lambda \mathcal{E}(+0) - \lambda \mathcal{E}(+i0) = \frac{i}{2} \int d^3\mathbf{x} J(\mathbf{x}) [\partial_t \phi_{\text{cl}}(+0, \mathbf{x}) + \partial_t \phi_{\text{cl}}(+i0, \mathbf{x})], \quad (2.10)$$

where Eqs. (2.6) were used in the last equality. Now, it is clear that $\partial_t \phi_{\text{cl}}$ should become singular at $t = 0$ in the limit $J \rightarrow 0$, or the energy E would vanish.

Another clarification of the analytic structure comes from the solution at $\lambda n = \lambda E = 0$ and $J = 0$ which is known analytically [5, 54]. It is spatially homogeneous:

$$\phi_{\text{cl}}(t, \mathbf{x}) = -im\sqrt{2}/\sin(mte^{i\epsilon'}) \quad \text{at} \quad \lambda n = \lambda E = 0, \quad (2.11)$$

where $\epsilon' \rightarrow +0$ is a regulator. One can check that Eq. (2.11) solves the field equation with zero source, has $a_{\mathbf{k}} = 0$, and satisfies the boundary conditions (2.2), (2.3), and (2.4) at $\theta = +\infty$. Expressions (2.5) then give zero quantum numbers of the final state. We see a singularity of ϕ_{cl} at $t = 0$ — or, rather, a flat three-dimensional singularity hyperplane in the four-dimensional spacetime. But the configuration (2.11) is also singular at the chain of points $t = \pi k e^{-i\epsilon'}/m$ with integer k which reside somewhat below the real time axis at $k > 0$. Below we will demonstrate numerically that the spatial homogeneity of solutions is broken at nonzero E and n , but the qualitative singularity structure remains. Namely, the singularities form [9, 54] chains of hypersurfaces $t = t_*(\mathbf{x})$, $t'_*(\mathbf{x})$, etc. shown in Fig. 3b. The first — “main” — hypersurface $t_*(\mathbf{x})$ passes the point $t_* = \mathbf{x} = 0$ at $J = 0$ and shifts to $\text{Im } t_* < 0$ at nonzero source. This corresponds to singular and regular solutions on the contour A0B, respectively. We pictured the “main” singularity in Fig. 3b by the solid ($J = 0$) and dashed ($J \neq 0$) lines starting at the crossed circles.

It is worth noting that the original paper [54] took one step forward and tried to derive boundary value problem for the actual singular solutions at $J = 0$. We will not use such reformulation, as it is inconvenient for numerical implementation.

To sum up, our semiclassical method consists of solving Eqs. (2.1) — (2.5) and evaluating the exponent (2.7). The last step is extrapolation of results to $J \rightarrow 0$ according to Eq. (1.5), which will be also done numerically.

2.2 Numerical implementation

Now, we reformulate the semiclassical boundary value problem on the lattice. We switch to dimensionless units with $m = 1$ and consider a Gaussian source

$$J(\mathbf{x}) = j_0 e^{-\mathbf{x}^2/2\sigma^2} \quad (2.12)$$

of strength j_0 and width σ . Eventually, we will send $j_0 \rightarrow 0$ and $\sigma \rightarrow 0$ at a fixed j_0/σ . This will make the source local in space and small in amplitude, i.e. similar to the vanishing delta function $J \rightarrow (2\pi)^{3/2} j_0 \sigma^3 \delta^{(3)}(\mathbf{x})$ used in [54]. Comparing results at different j_0/σ , we will test universality of the semiclassical exponent.

We assume spherical symmetry of the saddle-point configurations: $\phi_{\text{cl}} = \phi_{\text{cl}}(t, r)$, where $r \equiv |\mathbf{x}|$. This Ansatz passes the saddle-point equations (2.1) — (2.5) and agrees with all previously known semiclassical solutions [9, 54, 61]. Spherical symmetry also complies with insensitivity of the semiclassical exponent to the few-particle initial state: taking the latter isotropic, one can make the entire process rotationally invariant. On the other hand,

the spherical Ansatz leaves only two coordinates t and r and hence significantly simplifies numerical calculations.

We introduce temporal and spatial lattices with sites t_j and r_i covering the complex contour³ A0B in Fig. 3b and a finite spherical box $0 \leq r_i \leq R$, where $-1 \leq j \leq N_t + 1$ and $0 \leq i \leq N_r - 1$. The complex field $\phi_{j,i} \equiv \phi_{\text{cl}}(t_j, r_i)$ is stored at the lattice sites. We considerably decrease the time steps $|t_{j+1} - t_j|$ near the origin $t = 0$, i.e. in the vicinity of the “main” singularity. On the other hand, our spatial lattice is uniform. Practice shows that this choice is optimal for achieving reasonable accuracy at restricted computational resources.

We discretize the boundary value problem using the standard second-order scheme, see Appendix A for details. To this end we notice that the field equation (2.1) can be obtained by extremizing the classical action with the source term,

$$S_J = S[\phi] + \frac{i}{\lambda} \int d^3\mathbf{x} J(\mathbf{x}) \phi(0, \mathbf{x}). \quad (2.13)$$

Discretizing the latter functional, we arrive at a nonlinear function S_J of $\phi_{j,i}$ and the lattice field equation

$$G_{j,i} \equiv \frac{\partial S_J}{\partial \phi_{j,i}} = 0. \quad (2.14)$$

The Dirichlet boundary condition in the infinite past (2.2) can be imposed at the very first time site $t = t_{-1}$ — the point A of the time contour: $\phi_{-1,i} = 0$. Numerical implementation of the condition in the asymptotic future (2.4) is far less trivial. In Appendix A we show that it relates the field values at the two very last time sites $t = t_{N_t}$ and t_{N_t+1} . Indeed, in the continuous case $a_{\mathbf{k}}$ and $b_{\mathbf{k}}^*$ can be obtained by Fourier-transforming ϕ_{cl} and $\partial_t \phi_{\text{cl}}$ and taking appropriate linear combinations of their images, see Eq. (2.3). On the lattice, one can express the field and its time derivative in terms of $\phi_{N_t,i}$ and $\phi_{N_t+1,i}$, thus turning Eq. (2.4) into a linear relation between them. The last two equations for the Lagrange multipliers T and θ are obtained by substituting lattice versions of $a_{\mathbf{k}}$ and $b_{\mathbf{k}}^*$ into Eqs. (2.5). Finally, the result for F_J is given by Eq. (2.7) with the discretized action.

To sum up, our lattice formulation of the semiclassical boundary value problem includes $2N_r(N_t + 3) + 2$ real nonlinear equations for the same number of unknowns $y_\alpha \equiv \{\text{Re } \phi_{j,i}, \text{Im } \phi_{j,i}, T, \theta\}$. We solve them using Newton-Raphson numerical method [64]. Namely, suppose a crude approximation $y_\alpha^{(0)}$ to the solution is known. Then the correction $\delta y_\alpha = y_\alpha - y_\alpha^{(0)}$ satisfies the linear system

$$G_\alpha(y^{(0)}) + \sum_\beta \delta y_\beta \left. \frac{\partial G_\alpha}{\partial y_\beta} \right|_{y^{(0)}} = 0, \quad (2.15)$$

where G_α are the left-hand sides all lattice equations: Eq. (2.14), the boundary conditions, and equations for T and θ . Once Eqs. (2.15) are solved, we refine the approximation, $y_\alpha^{(0)} \rightarrow y_\alpha^{(0)} + \delta y_\alpha$, and solve them, again, until the procedure converges. Note that the

³At large λn the chain singularities of the solutions approach the real time axis and inflate numerical errors. In that case we deform the “Minkowskian” part of the time contour to the line 0B'B shown in Fig. 3b (dotted).

Newton-Raphson method is very picky to the first choice of $y^{(0)}$, but converges quadratically fast [64] if the latter is sufficiently close to the solution. We will discuss selection of that configuration in the next section.

Computationally, the most time-consuming part of the problem is to solve the sparse linear system (2.15). We do this using the elimination algorithm of Refs. [26, 36] and GPU-accelerated linear algebra package [65].

In practical computations we fixed $N_r = 256$ and varied the size of the spatial box between $R = 100$ at $\varepsilon = 0.35$ and $R = 6.5$ at $\varepsilon = 5$; recall that $m = 1$ in our units. This allowed us to encompass long-wave parts of nonrelativistic configurations and, in the case of large ε , resolve high-frequency modes of more compact and energetic solutions. The time steps were $|\Delta t| \sim 10^{-2} \div 10^{-3}$ near the ends of the contour and two orders of magnitude smaller near $t = 0$. We always selected the Minkowskian contour length t_{N_t+1} comparable to R because out-waves move inside the lightcone. The Euclidean part $|\text{Im } t_{-1}|$ was shorter than that by a factor of few. The resulting temporal lattices had $N_t = 7061 \div 12201$ sites.

We controlled numerical precision by changing the lattice parameters N_r , R , N_t , $\text{Im } t_{-1}$, and t_{N_t+1} . This had led to variability of the suppression exponent of order 10^{-3} in the center of the parameter region and up to 2% in the worst cases. The errors were mainly coming from the finite size and spatial discretization effects, while dependence on the temporal lattice was ten times weaker. The absolute accuracies of T and θ were always better than 10^{-2} , and relations (2.8) held to the same precision. We monitored the conservation of energy (2.9) on the Euclidean and real-time parts of the contour. It remained stable at the 1% level except for the cases of the lowest and highest ε when 6 \div 24% nonconservation was observed near $t = 0$. Linearization of the out-waves was checked by comparing the exact and linear energies, Eqs. (2.9) and (2.5), respectively, at $t \approx t_{N_t+1}$, i.e. at the point B of the time contour. The relative deviation of these quantities was always smaller than 0.4%.

It is worth noting that all numerical artefacts described above are subdominant with respect to the extrapolation errors originating from evaluation of the limits $J \rightarrow +0$, $\lambda n \rightarrow +\infty$, and $\varepsilon \rightarrow 0$. Errorbars on the plots display the latter inaccuracies.

3 A way to singular solutions

The above numerical technique allows one to reconstruct the entire branch of saddle-point configurations from a single representative solution. Indeed, let $y_\alpha^{(0)} = \{\phi_{\text{cl}}^{(0)}(t, \mathbf{x}), T^{(0)}, \theta^{(0)}\}$ is a solution with parameters $\lambda n^{(0)}$, $\varepsilon^{(0)}$, $j_0^{(0)}$, and $\sigma^{(0)}$, where the last two values characterize the Gaussian source $J(\mathbf{x})$. Slightly changing one or several parameters, e.g. $\varepsilon = \varepsilon^{(0)} + \delta\varepsilon$, we numerically search for the new solution y_α using $y_\alpha^{(0)}$ as the first approximation. If the change of parameters is small enough, the approximation is good and the iterative method converges. After that we reload $y^{(0)}$ with the newly found solution and repeat the procedure, making another step in the parameter space and finding yet another solution, etc. In this way we can cover all accessible parameter region with solutions.

The question is: where to get the very first configuration $y^{(0)}$? We need a physical one giving the dominant contribution to the path integral for the probability.

It is clear that in a certain regime the quartic interactions are irrelevant and the particles in the final state are created by the classical source $J(\mathbf{x})$. This situation is opposite to the target limit $J \rightarrow 0$ when all particles are produced by the interaction vertices and the result is insensitive to the source profile. Ignoring the ϕ_{cl}^3 term in the field equation (2.1), we obtain the semiclassical solution in the linear theory,

$$\phi_{\text{cl}}^{(\text{lin})}(t, \mathbf{x}) = - \int \frac{d^3 \mathbf{k}}{(2\pi)^3} \frac{J^*(\mathbf{k})}{2\omega_{\mathbf{k}}} e^{i\omega_{\mathbf{k}}t - i\mathbf{k}\mathbf{x} + \theta - 2\omega_{\mathbf{k}}T} - i \int \frac{d^4 k}{(2\pi)^4} \frac{J(-\mathbf{k}) e^{ikx}}{k^2 - m^2 + i0}, \quad (3.1)$$

where the first term satisfies the homogeneous equation and the second equals Feynman's Green function convoluted with the source; $J(\mathbf{k})$ is a Fourier image of the latter. Hereafter we assume that this solution is continued analytically from the parts $t < 0$ and $t > 0$ of the real time axis to the intervals A0 and 0B of the complex contour in Fig. 3b, see explicit expressions in Appendix B. It is straightforward to check that Eq. (3.1) satisfies the boundary conditions (2.2) and (2.4) in the asymptotic past and future. Indeed, its two terms both vanish exponentially as $t \rightarrow +i\infty$ but represent different, positive- and negative-frequency components of ϕ_{cl} as $t \rightarrow +\infty$. As usual, the parameters T and θ are related to λn and ε by Eqs. (2.5), and the suppression exponent F_J is obtained by substituting Eq. (3.1) into Eq. (2.7) in the non-interacting case; see Appendix B for details.

It is clear that the above linear solution is proportional to the amplitude j_0 of the source, whereas λn and λE are quadratic in the field and thus proportional to j_0^2 . The interaction term $\phi_{\text{cl}}^3 \propto j_0^3$ in the equation is hence irrelevant in the limit of

$$\text{linear theory:} \quad j_0 \rightarrow 0, \quad \lambda n \propto j_0^2 \quad \text{at fixed } \varepsilon \text{ and } \sigma. \quad (3.2)$$

We thus expect that at small j_0 and λn the configuration (3.1) approximately satisfies the full nonlinear boundary value problem.

Importantly, the solution in the free theory is unique and definitely physical⁴, as the path integral in this case is Gaussian. We therefore use Eq. (3.1) as the very first approximation for the numerical procedure described above. Namely, setting $y_\alpha^{(0)} = \{\phi_{\text{cl}}^{(\text{lin})}, T^{(\text{lin})}, \theta^{(\text{lin})}\}$ at sufficiently small j_0 , $\lambda n \sim O(j_0^2)$, and finite σ and ε , we observe that the iterations converge fast to the nonlinear solution with the same parameters. Computing the suppression exponent F_J of the latter, we display it with the circle S_0 in Fig. 4a. After that we start increasing j_0 and $\lambda n \propto j_0^2$ in small steps and finding numerical solutions at every step, until the configurations with $\lambda n \sim O(1)$ are obtained; see the chain of circles S_0S leading to the solution S in the figure. The configurations with large j_0 and λn are visibly different from the ones in the free theory; we will discuss them in the next Section. In Fig. 4a we compare their

⁴We checked this explicitly: calculated the matrix elements $\langle f; E, n | \exp\{-\int d^3 \mathbf{x} J \hat{\phi} / \lambda\} | 0 \rangle$ using the algebra of creation and annihilation operators in the linear theory and then performed the final-state sum in Eq. (1.1) via the steepest descent method. The resulting value of F_J coincided with that for the semiclassical solution (3.1).

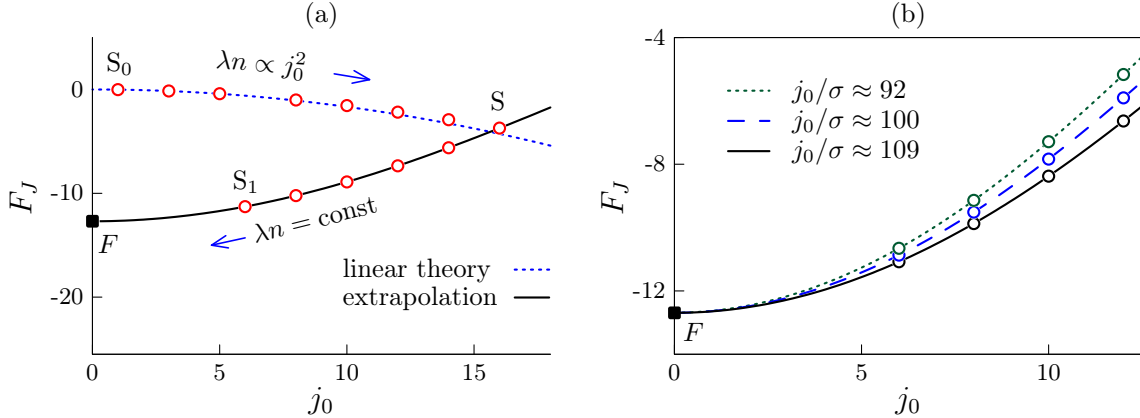


Figure 4: (a) The exponent F_J versus the source strength j_0 at $\varepsilon = 3$. The chain S_0S of solutions (circles) is obtained by increasing j_0 at given $\lambda n/j_0^2 \approx 10^{-2}$ and $\sigma \approx 0.13$, while the solutions from the lower branch SS_1 (also circles) have fixed $\lambda n \approx 2.51$ and $j_0/\sigma \approx 120$. Dotted and solid lines show the suppression exponent (B.4) in the linear theory and the polynomial extrapolation (3.4) to $j_0 = 0$, respectively. (b) Extrapolations $j_0 \rightarrow 0$ at different j_0/σ for $\varepsilon = 3$ and $\lambda n = 2.51$ (lines passing through the data circles). We use units with $m = 1$.

suppression exponents with the prediction of the linear theory (dotted line and Eq. (B.4) from Appendix B). As expected, the two graphs are close at small j_0 but start to deviate at large values of this parameter.

Independently changing the parameters λn , ε , j_0 , and σ in small steps, we reproduce the entire continuous branch of numerical solutions and compute the exponent F_J .

The final but nontrivial part of our procedure consists of evaluating the few-particle limit $J \rightarrow 0$ or, more precisely,

$$\text{few-particle: } j_0 \rightarrow 0, \quad \sigma \propto j_0 \quad \text{at fixed } \varepsilon \text{ and } \lambda n. \quad (3.3)$$

We have already argued that the semiclassical configurations become singular in this limit. They cannot be resolved on the lattice. Say, the lower branch SS_1 of numerical solutions in Fig. 4a (circles) is obtained from S by decreasing j_0 in accordance with Eq. (3.3). The last representative S_1 of this branch already has poor precision, and solutions at even smaller j_0 cannot be obtained with acceptable accuracy. We will explicitly visualize the singularities of the solutions below.

A way out is to extrapolate results to $j_0 = 0$ using valuable analytic input summarized in Appendix C. Indeed, it is clear [54] that weak and narrow source affects the solutions locally in the vicinity of $(t, \mathbf{x}) = 0$ making them regular, i.e. slightly shifting their “main” singularities $t_*(\mathbf{x})$ to the lower complex time plane, see the dashed line with the crossed circle in Fig. 3b. Analyzing the solutions near the singularity, we can extract their dependence on j_0 . In Appendix C we argue that the saddle-point configuration itself, its Lagrange

multipliers T , θ , and the exponent F_J can be expressed as power series in j_0^2 ; e.g.,

$$F_J(\lambda n, \varepsilon) = F + F_1 j_0^2 + F_2 j_0^4 + F_3 j_0^6 + \dots, \quad (3.4)$$

where the coefficients $F_i(\lambda n, \varepsilon)$ are independent of j_0 .

In practice, for every chosen λn and ε we compute the solutions at several small values of j_0 but the same j_0/σ . Then we fit their exponents F_J and the parameters T , θ with cubic polynomials of j_0^2 , i.e. the four first terms in Eq. (3.4). This procedure is illustrated in Fig. 4a where Eq. (3.4) (solid line) correctly describes the numerical data SS_1 (circles). The few-particle exponent F and the respective values of T and θ are given by the first coefficients of the polynomials (filled square F in the figure).

We finish this Section with the test of the suppression exponent universality. Recall that the universality conjecture [22, 23] declares insensitivity of F to the few-particle initial state, in particular, to the profile of the vanishingly small source $J(\mathbf{x})$ and its relative width σ/j_0 . In Fig. 4b we confirm that this is the case, indeed. Namely, performing three independent polynomial fits (lines) of the data with different j_0/σ (circles), we arrive at the same result for F (filled square). It is worth stressing that the universality assumption lies in the basis of our semiclassical method [54].

Note that the extrapolation $J \rightarrow 0$ generates the largest errors in our numerical procedure. We estimate them by changing the numbers of data points and j_0 intervals in the fits. The respective scatter of the extrapolation results essentially depends on ε and λn and is highly sensitive to the discretization errors adding a pseudorandom component to the data. Typically, the final result for F is stable within 0.7% precision interval which, however, grows to 6% at the highest and lowest ε and largest multiplicities. The accuracy of the extrapolated T and θ is better than 8% in the center of our parameter region but deteriorates to 13 – 20% for the smallest⁵ ε and λn . We display extrapolation errors with errorbars in plots whenever they are larger than the point size.

4 Numerical results

4.1 Semiclassical solutions

In Fig. 5 we display the saddle-point solution with relatively small out-state multiplicity $\lambda n \approx 0.63$ and low kinetic energy $\varepsilon = 0.5$, see also the movie [66(a)] and recall that $m = 1$ in our units. Three-dimensional surface in this figure shows the absolute value of ϕ_{cl} as a function of the radial coordinate r and a parameter $\text{Re } t - \text{Im } t$ along the time contour⁶ A0B, while the color marks complex phase of ϕ_{cl} . We see that the solution decreases exponentially towards the left side of the graph, i.e. as $t \rightarrow +i\infty$. Besides, it has a sharp peak near the origin $t = r = 0$ where the weak source $J(\mathbf{x})$ is situated. Note that the latter source is nonzero in all our visualized configurations. At $t > 0$ the solution in Fig. 5 describes complex-valued

⁵Formally, the relative error of T exceeds 100% at high ε where this parameter is small.

⁶We never show solutions along the deformed contour A0B'B; cf. Fig. 3b.

outgoing wave packet that moves inside the light cone. Figure 6 demonstrates two solutions with other values of λn and ε .

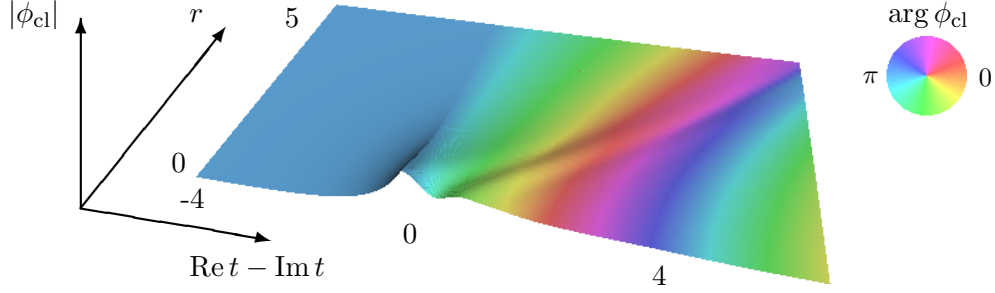


Figure 5: Semiclassical solution with $\lambda n \approx 0.63$, $\varepsilon = 0.5$, $j_0 = 0.6$, and $\sigma \approx 0.18$ in units with $m = 1$. Color indicates complex phase of ϕ_{cl} .

The solutions in Figs. 5 and 6 have relatively large j_0 and are still far from being singular. Their parts near the origin $t = r = 0$, however, strongly depend on the source and turn into high and narrow peaks once the value of j_0 gets smaller. Indeed, in Appendix C we derive general form of solutions near their singularities $t = t_*(r)$ [cf. Eq. (2.11)],

$$\phi_{\text{cl}} \approx \frac{-i\sqrt{2}}{t - t_*(r)}, \quad t_*(r) = t_{*,0} + t_{*,2}r^2 + O(r^4) \quad \text{at small } |t - t_*|, r \text{ and small } j_0, \quad (4.1)$$

where $t_{*,k}$ are generic Taylor coefficients. We confirm this prediction in Fig. 7a. Namely, our numerical solution (circles) is correctly described by Eq. (4.1) (line) at $t = +0$ and small r .

Moreover, in Appendix C we also argue that $t_*(0) = O(j_0^2)$ at small j_0 and finite j_0/σ . This means that the “tip” of the singularity surface marked by the cross in Fig. 3b touches

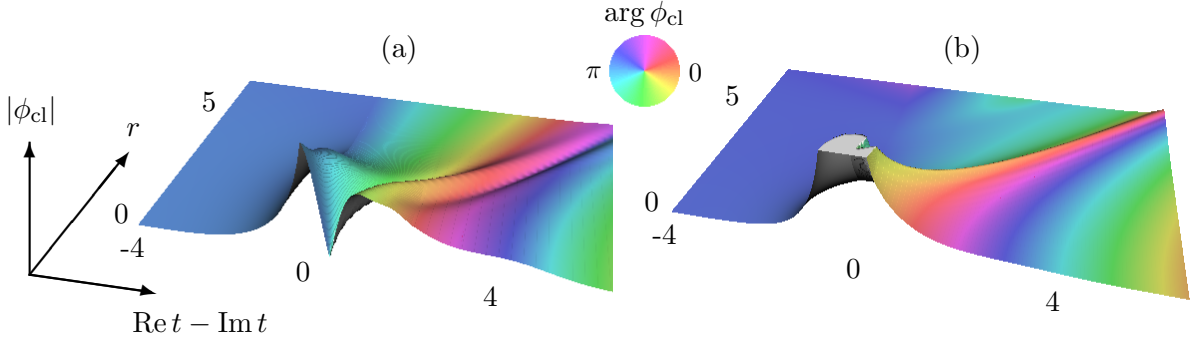


Figure 6: Two semiclassical solutions obtained from the one in Fig. 5 by increasing (a) the out-state multiplicity λn and after that — (b) the mean energy ε of out-particles. The peak of the solution (b) at $t, r \approx 0$ is cropped off for visualization purposes. The parameters of the solutions are (a) $\lambda n \approx 18.8$, $\varepsilon = 0.5$, $j_0 = 7.8$, $\sigma \approx 0.41$ and (b) $\lambda n \approx 18.8$, $\varepsilon = 3$, $j_0 = 12$, $\sigma \approx 0.2$. Recall that the color encodes complex phase of $\phi_{\text{cl}}(t, r)$ and we exploit units with $m = 1$.

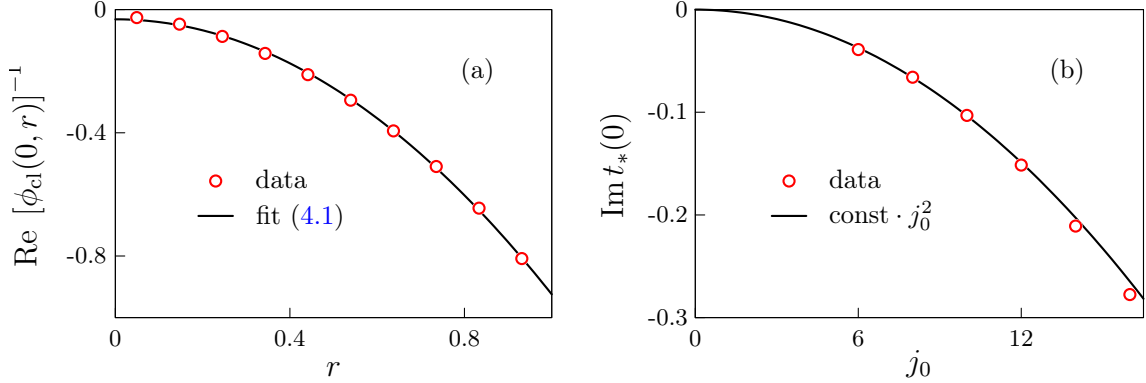


Figure 7: (a) Inverse field $\text{Re} [\phi_{\text{cl}}(0, r)]^{-1}$ at $t = +0$ and small r . Numerical data (circles) are fitted with quadratic polynomial in Eq. (4.1) (line). The solution has parameters $\lambda n \approx 2.51$, $\varepsilon = 3$, $j_0 = 6$, and $\sigma = 0.05$. (b) The tip $t_*(0)$ of the “main” singularity surface versus j_0 . This graph corresponds to $j_0/\sigma = 120$ and the same out-state parameters as in Fig. (a). The solid line is a parabola $t_*(0) \propto j_0^2$. Units with $m = 1$ are used in both figures.

the origin $t = 0$ in the limit of vanishing source. To check the latter behavior, we computed the singularities $t_*(0)$ of our numerical solutions. Namely, we solved the field equation along the imaginary time axis from $t = +0$ to $\text{Im} t < 0$ until $\phi_{\text{cl}}(t, 0)$ became comparatively large, and then fitted its time dependence with Eq. (4.1). The resulting values of $t_*(0)$ (circles in Fig. 7b) are proportional to j_0^2 (line), indeed.

With growth of λn , the solutions become visibly larger in size and more nonlinear in the region of finite $|t|$ and r , see Fig. 6a. Besides, they develop extra peaks near the second singularity surfaces $t'_*(r)$ from the chain in Fig. 3b. This last property suggests that the additional singularities come closer to the real time axis and start to affect the field evolution. Also, at $\lambda n \gg 1$ the amplitudes of the out-waves are visibly larger. We observe the following scaling in the linear region:

$$\phi_{\text{cl}}(t, r) \approx \sqrt{\lambda n} \cdot \tilde{\phi}(t, r) \quad \text{at} \quad t \rightarrow +\infty \quad \text{and} \quad \lambda n \gg 1, \quad (4.2)$$

where $\tilde{\phi}$ does not depend on the multiplicity. Indeed, let us have a look at the rescaled final-state occupation numbers $a_{\mathbf{k}} b_{\mathbf{k}}^*/(\lambda n)$ in Fig. 8, where $\int d^3 \mathbf{k} a_{\mathbf{k}} b_{\mathbf{k}}^* = \lambda n$. Their dependence on the particle energy $\omega_{\mathbf{k}}$ has the same form at essentially different λn in accordance with the above prediction.

We envision that the asymptotic property (4.2) may be valid in a wide class of models. Besides, the distribution of the out-particles in Fig. 8, which is independent of n , may serve as a useful benchmark signature for multiparticle production, if the latter will be ever considered in the experimental context.

The above scaling is no longer valid in the interaction region where the ϕ^3 term of the field equation (2.1) cannot be neglected. Indeed, the Ansatz (4.2) would make this term dominant and uncompensated in the limit $\lambda n \rightarrow +\infty$. We estimate the size r_{int} of the

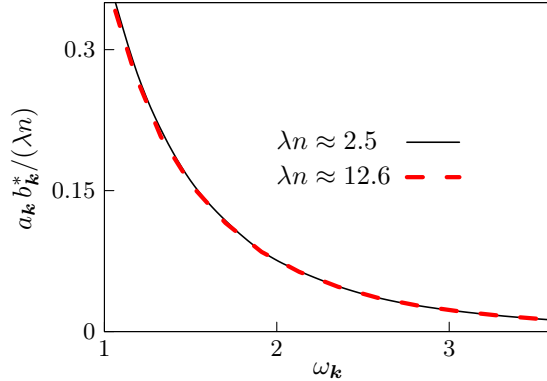


Figure 8: Rescaled occupation numbers $a_{\mathbf{k}} b_{\mathbf{k}}^*/(\lambda n)$ of the final state versus the particle energy $\omega_{\mathbf{k}}$. The two graphs correspond to $\lambda n \approx 2.51$ and $\lambda n = 12.57$ at $\varepsilon = 3$ and $j_0 = 0$. We use units with $m = 1$.

nonlinear region by observing that at $\varepsilon \gtrsim O(m)$ the out-waves go away with decreasing amplitudes $\phi_{\text{cl}} \propto \sqrt{\lambda n}/r$ roughly along the lightcone $r \sim t$. Then the ϕ^3 term is essential in

$$\text{the interaction region: } r \lesssim r_{\text{int}} \sim \frac{\sqrt{\lambda n}}{(\varepsilon^2 + 2m\varepsilon)^{1/2}} \quad \text{and} \quad t \lesssim r_{\text{int}}. \quad (4.3)$$

This expectation is supported by our numerical results. In particular, Fig. 9a shows the inverse field $|\phi_{\text{cl}}(0, r)|^{-1}$ at $t = 0$ as a function of r/r_{int} for three large values of λn . With growth of multiplicity, the graphs at $r < r_{\text{int}}$ approach a particular almost flat profile of height $\phi_{\text{cl}}^{-1} \lesssim m^{-1}$. Recall that small value of $\phi_{\text{cl}}^{-1}(0, r)$ estimates the position $t_*(r)$ of the singularity surface which is, therefore, also flat at large λn and $r \lesssim O(\lambda n)^{1/2}$; see Eq. (4.1). At $r \sim r_{\text{int}}$ and beyond this point, the graphs in Fig. 9a sharply increase indicating entrance into the linear region with small ϕ_{cl} .

We visualize the nonlinear stage of evolution by showing the energy density $|\rho_{\mathcal{E}}|$ of the solution — the integrand in Eq. (2.9) — at different moments of time t in Fig. 9b. Apparently, the source and the nearby singularity create a huge localized peak of $\rho_{\mathcal{E}}$ at $t = 0$ which evolves to larger r remaining narrow and essentially interacting until it crosses the boundary $r_{\text{int}} \propto \sqrt{\lambda n}$ of the nonlinear region (dotted vertical line). At $r \sim r_{\text{int}}$ the peak quickly linearizes and starts to satisfy Eq. (4.2), see the graph with $t = 5m^{-1}$ in Fig. 9b. Such nonlinear evolution of a narrow shock supports the “thin wall” Ansatz suggested in Ref. [58] and used in the papers on “Higgsplosion” [39, 40].

Figure 6b demonstrates the solution with high mean energy ε of the out-particles. This configuration is essentially sharper and has narrow outgoing wave packet localized on the light cone $r \sim t$. One may assume that such solutions with $\varepsilon \gg m$ can be obtained in the massless theory, and the parameter m^2 can only cause their small deformation. We will further justify this observation in the next Section.

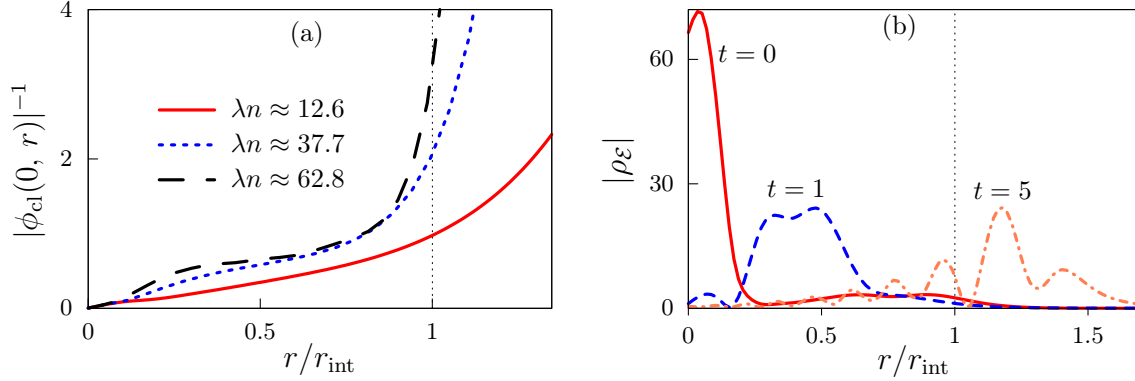


Figure 9: (a) Inverse field $|\phi_{\text{cl}}(0, r)|^{-1}$ as a function of the rescaled radial coordinate r/r_{int} at $t = 0$. All the graphs have $\varepsilon = 1$, $j_0 = 12$, and $\sigma \approx 0.19$. (b) Energy density $|\rho_\varepsilon|$ depending on r/r_{int} for the solution with $\lambda n \approx 37.7$. The other parameters are the same as in Fig. (a). Units with $m = 1$ are used.

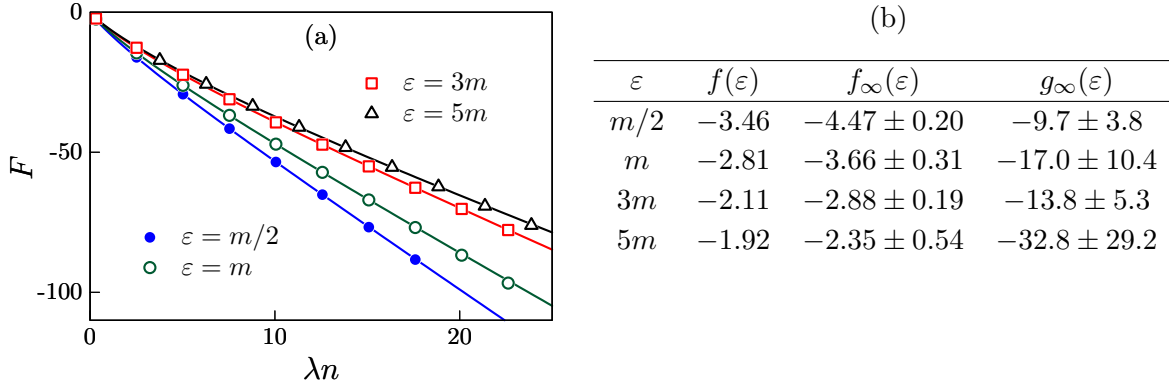


Figure 10: (a) Suppression exponent F as a function of λn at fixed ε . Points demonstrate numerical data, lines are the fits (4.5). (b) Parameters in Eq. (4.5).

4.2 Suppression exponent

We had already presented main results for the exponent $F(\lambda n, \varepsilon)$ in the Introduction. Here we study its asymptotic, fit the data with convenient formulae, and show remaining numerical results in Fig. 10a (points). Recall that we confirmed universality of the exponent in Sec. 3 and Fig. 4b.

Start with the regime $\lambda n \ll 1$. It corresponds to perturbative limit because the series in λn can be viewed as expansion in λ . Main contributions in this case come from the tree-level diagrams giving [5, 8, 54],

$$\text{tree: } F(\varepsilon, \lambda n) = \lambda n \ln \frac{\lambda n}{16} - \lambda n + f(\varepsilon) \lambda n + O(\lambda n)^2, \quad (4.4)$$

where $O(\lambda n)^2$ contains loop corrections and the function $f(\varepsilon)$ is computed numerically in

Ref. [61]. We determine $f(\varepsilon)$ using half-analytic $O(4)$ approximation of Ref. [62] which works extremely well [61] in our parametric region $\varepsilon \leq 5m$. Results for this function are tabulated in the first column of Fig. 10b. The overall tree-level exponent (4.4) is shown at $\varepsilon = 3m$ in Fig. 2a (dotted line). As expected, it is close to the numerical data (circles) at $\lambda n \ll 1$.

We performed more indicative comparison with the perturbative results in the accompanying paper [53]. In there, we extracted $f(\varepsilon)$ by fitting the numerical data for F at small λn with Eq. (4.4). The result agreed with the tree-level exponent of Refs. [61, 62].

In the opposite limit of large λn the tree-level exponent (4.4) becomes positive which may be naively taken [1, 2] for a signal of unsuppressed multiparticle production. But in fact, the value of F is dominated at $\lambda n \gtrsim 1$ by loop corrections and has the opposite behavior: it decreases monotonically with the multiplicity and approaches the linear asymptotic (1.6) at $\lambda n \gg 1$, see Fig 2a. The slope $f_\infty(\varepsilon) < 0$ and shift $g_\infty(\varepsilon)$ of the asymptotic strongly depend on ε , cf. Fig. 2b. In practice, it is convenient to approximate the numerical data at finite λn and ε with the interpolating formula

$$F \approx \lambda n f_\infty(\varepsilon) - \frac{\lambda n}{2} \ln \left[\left(\frac{16}{\lambda n} \right)^2 e^{2-2f(\varepsilon)+2f_\infty(\varepsilon)} - \frac{2g_\infty(\varepsilon)}{\lambda n} + 1 \right], \quad (4.5)$$

which reduces to Eqs. (4.4) and (1.6) in the limits of small and large multiplicity. Indeed, fits with Eq. (4.5) (lines in Fig. 10a) pass through all the data points. The best-fit values of $f_\infty(\varepsilon)$ and $g_\infty(\varepsilon)$ are tabulated in Fig. 10b and plotted in Fig. 2b. We checked that they are consistent with the results of simple linear fits⁷ (1.6) at $\lambda n \gg 1$. Note also that $f(\varepsilon)$ is fixed by an independent tree-level calculation and remains constant in the fits.

Now, consider the limit $\varepsilon \rightarrow 0$ in which all final particles are produced at the mass threshold. The scattering amplitude \mathcal{A}_n is expected to have a finite limiting value corresponding to zero outer momenta [5, 11–14]. Then the inclusive probability factorizes at low ε into $\mathcal{P}_n \approx |\mathcal{A}_n|^2 \mathcal{V}_n/n!$, where [54]

$$\frac{\mathcal{V}_n}{n!} \approx \frac{m^{2n-4}}{n!} \exp \left\{ \frac{3n}{2} \ln \left(\frac{\varepsilon}{3\pi m} \right) + \frac{3n}{2} - n \ln 2 + \frac{n\varepsilon}{4m} \right\}, \quad \varepsilon \ll m \quad (4.6)$$

is the total phase volume of n identical nonrelativistic particles. Using the above observation, we extract the exponent $F_{\mathcal{A}}$, Eq. (1.8), of the amplitude from the probability as follows:

$$F_{\mathcal{A}}(\lambda n) = \frac{1}{2} \lim_{\varepsilon \rightarrow +0} [F(\lambda n, \varepsilon) - \lambda \ln(\mathcal{V}_n m^{4-2n})]. \quad (4.7)$$

With the ideal data, one might be able to evaluate this limit directly, by fitting the combination in the right-hand side with polynomials of ε and extracting constant terms. But that is

⁷We performed another strong test of Eq. (4.5). Relations (2.7) and (2.8) give the saddle-point value of the classical action in terms of the exponent and its λn derivative at $\varepsilon = \text{const}$: $2\lambda \text{Im} S[\phi_{\text{cl}}] = F - \partial F / \partial \ln(\lambda n)$, where $J = 0$. This expression turns Eq. (4.5) into an interpolating formula for $2\lambda \text{Im} S$. Approximating the numerical data at $J = 0$ with the latter, we extracted $g_\infty(\varepsilon)$ and $f_\infty(\varepsilon)$ which agreed with the values in Fig. 10b.

hard to do in practice, since our values of F already have essential inaccuracies due to previous extrapolation $j_0 \rightarrow 0$. We increase precision by recalling that the semiclassical procedure conveniently provides the ε derivative of the exponent $\partial F/\partial\varepsilon = 2\lambda nT$, see Eqs. (2.8). Recall that we obtain the values of T on par with the numerical solutions, and we also extrapolate them to $j_0 = 0$. It is straightforward to see that the $O(\varepsilon)$ term cancels out in the Taylor series expansion of the combination

$$F - \lambda \ln(\mathcal{V}_n m^{4-2n}) - 2\lambda n\varepsilon T + \lambda n(3/2 + \varepsilon/4m) = 2F_{\mathcal{A}} + \varepsilon^2 F_{\mathcal{A},2} + \varepsilon^3 F_{\mathcal{A},3} + O(\varepsilon^4) \quad (4.8)$$

because $\lambda\varepsilon\partial_\varepsilon \ln \mathcal{V}_n \approx \lambda n(3/2 + \varepsilon/4m)$ according to Eq. (4.6). Note that $F_{\mathcal{A}}$ in the right-hand side of Eq. (4.8) is our target exponent of the threshold amplitude and we denoted the other expansion coefficients by $F_{\mathcal{A},i}$. In practice, the three-parametric fit of the quantity in the left-hand side of Eq. (4.8) with the sparse polynomial in the right-hand side is much more stable and leads to smaller errors than direct numerical evaluation of Eq. (4.7).

We thus arrive at the amplitude exponent $F_{\mathcal{A}}(\lambda n)$ shown by the circles in Fig. 3a. At $\lambda n \lesssim 10$ these data are close to the perturbative expression (dashed line),

$$F_{\mathcal{A}} = \frac{\lambda n}{2} [\ln(\lambda n/8) - 1] - \frac{(\lambda n)^2 3^{3/2}}{32\pi^2} \ln(2 + \sqrt{3}) + O(\lambda n)^3 \quad \text{at} \quad \varepsilon = 0, \quad (4.9)$$

which includes the tree-level result [5] (dotted line) and one-loop correction [6, 9] in the first and second terms, respectively. In the opposite case of large λn we expect linear asymptotic $F_{\mathcal{A}} \rightarrow \lambda n f'_\infty + g'_\infty$ previewed in Eq. (1.9). Hence, it is convenient to merge small- and large- λn behavior in a single interpolating formula [cf. Eq. (4.5)]

$$F_{\mathcal{A}} = \lambda n f'_\infty - \frac{\lambda n}{4} \ln \left[\left(\frac{8}{\lambda n} \right)^2 e^{2+4f'_\infty} - \frac{4g'_\infty}{\lambda n} + 1 \right], \quad (4.10)$$

which correctly describes all the numerical results (solid line in Fig. 3a). Best-fit values of f'_∞ and g'_∞ are given in Eq. (1.9).

Now, consider the limit of highly ultrarelativistic particles in the final state $\varepsilon \rightarrow +\infty$. The respective numerical solutions are sharper, and their time and space derivatives visibly grow with ε , see Fig. 6b. In this regime it is natural to treat the parameter m^2 in the field equation perturbatively. On dimensional grounds one finds,

$$T = \frac{T_{-1}}{\varepsilon} + T_3 \frac{m^2}{\varepsilon^3} + O(\varepsilon^{-5}), \quad \text{hence} \quad F = F_0 + 2\lambda n T_{-1} \ln \frac{\varepsilon}{m} - \lambda n T_3 \frac{m^2}{\varepsilon^2} + O(\varepsilon^{-4}), \quad (4.11)$$

where the dimensionless coefficients T_i in the series depend on λn and we used the Legendre relation $\partial F/\partial\varepsilon = 2\lambda nT$ in the second equality, cf. Eqs. (2.8). As we will prove later, F cannot decrease with energy, i.e. $T \geq 0$ and $T_{-1} \geq 0$. This is compatible with Eq. (4.11) only if $T_{-1} = 0$: otherwise, the suppression exponent would be positive and break unitarity at sufficiently high energies. We conclude that at $\varepsilon \rightarrow +\infty$ the exponent is ε -independent and $T \propto \varepsilon^{-3}$. The latter scaling is confirmed in Fig. 11.

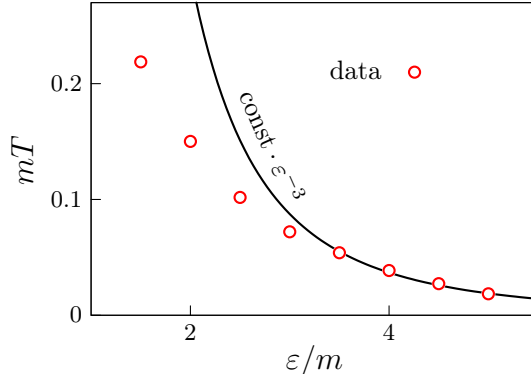


Figure 11: Lagrange multiplier T as a function of ε at $\lambda n \approx 18.8$ and $j_0 = 0$ (circles). Solid line demonstrates the asymptotic $T \propto \varepsilon^{-3}$ at large ε .

Since parametric behavior of the exponent at low and high ε is fixed, we can construct an interpolating formula for its dependence on energy or, equivalently, for its tilt $f_\infty = f_\infty(\varepsilon)$ at large λn . In practice we fit $f_\infty(\varepsilon)$ with the expression (1.7) that approaches a constant as $\varepsilon \rightarrow +\infty$ and a logarithm $\frac{3}{2} \ln(\varepsilon/m)$ from the phase volume at low ε . With the appropriately chosen parameters, this formula correctly describes all the numerical data, cf. the circles and the solid line in Fig. 2b.

We finish this Section with a remark that our numerical data are not limited to the four lines in Fig. 10a. In the ancillary files [63] we provide extra raw data at $\varepsilon/m = \{0.35, 0.75, 1.5, 2, 2.5, 3.5, 4, 4.5\}$ and different $\lambda n, j_0, \sigma$, results of their extrapolation to $j_0 = 0$, values of $f(\varepsilon)$ and best-fit results for f_∞ and g_∞ .

5 Discussion

In this paper we computed the probabilities of processes $\text{few} \rightarrow n$ in the unbroken $(3+1)$ -dimensional $\lambda\phi^4$ theory. To this end we numerically implemented D.T. Son’s semiclassical method of singular solutions. Our data cover a wide range of final-state multiplicities $n \gg 1$ and total collision energies E . They show that the multiparticle probabilities fall off monotonically with n and approach the decreasing exponent (1.6) at $n \gg \lambda^{-1}$. Up to our knowledge, no consistent calculation of this kind was performed before in a full-fledged field-theoretical model.

We have already presented main results in the Introduction. Here, we critically analyze their consistency. First, the probability (1.1) cannot exceed unity:

$$\mathcal{P}_n \sim e^{F/\lambda} \leq 1, \quad \text{and hence} \quad F(\lambda n, \varepsilon) \leq 0. \quad (5.1)$$

Note that breaking of Eq. (5.1) in any parametric region would undermine credibility of the entire method; cf. Eq. (1.2). But in reality it is satisfied by all our numerical data. In particular, the asymptotic of the exponent at large λn is negative: $F \rightarrow \lambda n f_\infty(\varepsilon) + g_\infty(\varepsilon) < 0$ at $\lambda n \rightarrow +\infty$, see Fig. 2b and table in Fig. 10b.

It is worth reminding that our semiclassical method relies on the universality conjecture [8, 20–27] for the exponent in Eq. (5.1). Namely, the value of $F(\lambda n, \varepsilon)$ does not depend on the details of the initial state as long as the latter includes few, i.e. $\ll \lambda^{-1}$, particles. We explicitly tested this assumption in Sec. 3, see Fig. 4b. Its consequence is that the cross section $\sigma_n \propto \exp(F/\lambda)$ of $2 \rightarrow n$ scattering is suppressed by the same universal function F as the probability \mathcal{P}_n . Indeed, consider a collision of two particles in a particular state described by wave packets with large spatial extent $L \gg n/E$. This collision creates n quanta with the probability⁸ $\mathcal{P}_n \sim \sigma_n/(\pi L^2)$, i.e. the same exponential suppression. The inequality (5.1) then means that the physical cross section σ_n cannot be exponentially large.

Second, consider the exotic process of two independent few-particle collisions creating n_1 and n_2 particles in two spatially separated regions. The overall probability for this to happen is $\mathcal{P}_{n_1}(E_1)\mathcal{P}_{n_2}(E_2)$, where E_1 and E_2 are the respective energies. In fact, such a two-collision event can be regarded as a subprocess contributing to the inclusive probability (1.1). Indeed, its initial state is not important by the universality conjecture and the final state including two widely separated particle sets is exclusive. Since $\mathcal{P}_n(E)$ is larger than the probability of a subprocess, we conclude [52],

$$F(\lambda n_1 + \lambda n_2, E_1 + E_2) \geq F(\lambda n_1, E_1) + F(\lambda n_2, E_2), \quad (5.2)$$

where the exponents are now expressed as functions of E instead of ε .

Using Eq. (5.2), it is easy to show that F grows with energy. Indeed, take $\lambda n_2 \ll 1$. Then the second collision is not exponentially suppressed at any E_2 : $F(\lambda n_2, E_2) \sim O(\lambda n_2)$ according to Eq. (4.4). The inequality (5.2) transforms into $F(\lambda n_1, E_1 + E_2) \geq F(\lambda n_1, E_1)$ implying that $\partial_E F \propto T$ is positive. Our numerical results do satisfy this criterion. Specifically, $f_\infty(\varepsilon)$ in Fig. 2b grows with ε and approaches the maximal value $f_\infty \rightarrow -2.57$ at $\varepsilon \rightarrow +\infty$.

Another particular case of Eq. (5.2) corresponds to a fixed mean energy of final particles $E_1/n_1 = E_2/n_2 = \varepsilon + m$ at arbitrary multiplicities. We obtain the inequality

$$F(\lambda n_1 + \lambda n_2, \varepsilon) \geq F(\lambda n_1, \varepsilon) + F(\lambda n_2, \varepsilon), \quad (5.3)$$

which means that the negative exponent cannot decrease at large multiplicities faster than linearly. Indeed, the power-law behavior $F \propto -(\lambda n)^\gamma$ is consistent with Eq. (5.3) at $\lambda n \rightarrow +\infty$ only if $\gamma \leq 1$. Our numerical calculation strongly suggests linear asymptotic $F \rightarrow \lambda n f_\infty + g_\infty$ that saturates this last condition. Then Eq. (5.3) reduces to $g_\infty(\varepsilon) \leq 0$ which is also true for our data, see the table in Fig. 10b.

Third, one may be surprised by the fact that the amplitude (1.9) of creating n particles at the mass threshold still grows factorially with n at $\lambda n \gtrsim 1$. This effect is purely kinematical and consistent with unitarity: recall that the amplitude was extracted from the exponentially small probability. Indeed, the factor $n!$ comes from the phase volume $\mathcal{V}_n/n!$

⁸This argument is rougher than the famous Froissart bound [67], as it assumes that the transition amplitude is insensitive to the scattering momenta at scales below L^{-1} . But it applies to our processes at a given n and large enough L because the inequality $|L^{-1} \partial_E \ln \mathcal{A}_n| \lesssim 1$ leads to $LE \gtrsim |d \ln \mathcal{A}_n / d \ln E| \sim (E \partial_E F)/\lambda \sim O(n)$.

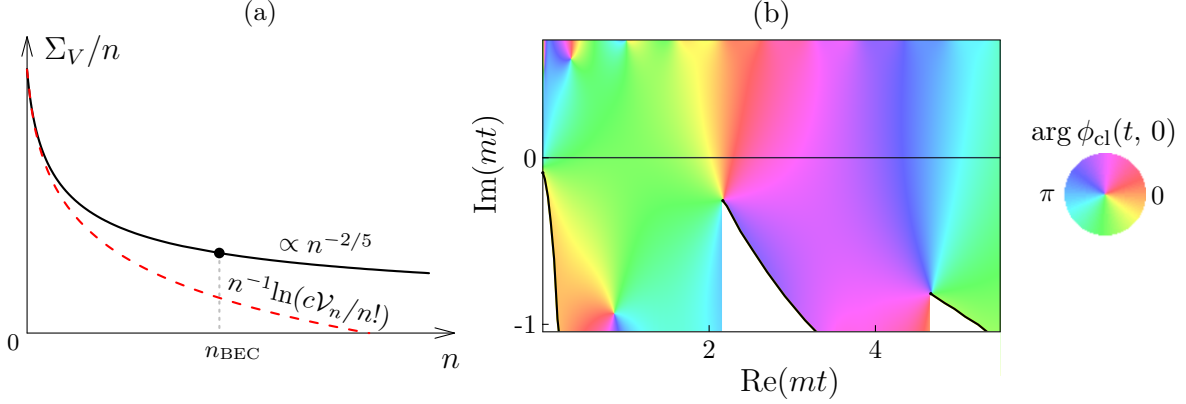


Figure 12: (a) Entropy $\Sigma_V(n, E)$ of n free nonrelativistic particles with total energy $E \approx nm$ in a finite volume V (solid line, not to scale). Dashed line is the logarithm of the phase volume (4.6). (b) Complex phase $\arg \phi_{\text{cl}}(t, 0)$ of the saddle-point configuration as a function of complex time at $r = 0$ (color). Black solid lines indicate singularities of ϕ_{cl} . We do not perform computations in the white regions below them. The solution has parameters $\lambda n = 2.51$, $\varepsilon = m/2$, $j_0 = 0.053 m^2$, and $\sigma = 0.29 m^{-1}$.

which has questionable physical interpretation in the limit $n \rightarrow +\infty$. To see this, consider a finite spatial volume V . The number of nonrelativistic n -particle states in that region is given by the exponent of the thermodynamical entropy $\exp\{\Sigma_V(n, E)\}$ (solid line in Fig. 12a). The latter, in turn, is proportional to the phase volume $\exp(\Sigma_V) = c\mathcal{V}_n/n!$ with coefficient $c \sim (2mV)^n/m^4$ (dashed line in the figure), but only at low multiplicities. At large $n \gtrsim n_{\text{BEC}}$ the wave functions of the gas particles start to overlap, Bose-Einstein condensation occurs, and the entropy stops being related to $\mathcal{V}_n/n!$ at all. To the contrary, it grows slowly [68], as $\Sigma_V \propto n^{3/5}$, with n because new states reluctantly appear in the overpacked Bose gas. In such a situation, the probability $\mathcal{P}_n \exp(-\Sigma_V)$ of transition to a given finite-volume state has almost the same suppression $F \sim \lambda n f_\infty < 0$ as the inclusive probability. We conclude that the threshold amplitude (1.9) should be interpreted with care at large n due to non-commutative nature of large-volume and large-multiplicity limits.

The above finite-volume picture resembles well-known result in quantum mechanics. Namely, consider one-dimensional particle in the potential $V_{QM}(x) = m_{QM}^2 x^2/2 + \lambda_{QM} x^4/4$. Its transition from the ground state to the n -th energy level occurs with the “probability” [56, 69]

$$\mathcal{P}_n^{(QM)} = |\langle n | \hat{O} | 0 \rangle|^2 \sim \exp \left\{ -\pi n + O(n^{1/3} \lambda_{QM}^{-2/3}) \right\} \quad \text{at} \quad n \gg O(\lambda_{QM}^{-1}), \quad (5.4)$$

where the prefactor is ignored and we assume that the operator \hat{O} does not depend on n . Amusingly, the asymptotic formula (5.4) does not involve the parameters λ_{QM} and m_{QM} of the potential. In this regard, it bears resemblance with our result for the multiparticle probability $\mathcal{P}_n \sim \exp\{n f_\infty + g_\infty/\lambda\}$ which is dominated at $\lambda n \gg 1$ by the λ -independent

factor $\exp\{nf_\infty\}$. Moreover, as we argued above, \mathcal{P}_n at large n can be interpreted as the probability of transition to one of the few accessible n -particle states in a large finite box. This makes the analogy even stronger. But there are significant differences. In field theory, the slope $f_\infty = f_\infty(\varepsilon)$ of the exponent depends on energy and the subdominant term $g_\infty(\varepsilon)/\lambda \sim O(n^0/\lambda)$ is different.

Forth, let us reproduce powerful argument [9, 37, 44] suggesting exponential suppression of multiparticle probabilities at arbitrary values of parameters: $F < 0$ at any $n \gg 1$ and E . Couple the scalar theory to the massless external fermions via Yukawa interaction $y\phi\bar{\psi}\psi$ with tiny coupling y . Then dispersion relation and optical theorem express the amputated Green's function $\Pi(Q^2)$ of two ϕ -operators in terms of the total fermion annihilation cross section $\sigma_{\text{tot}}(E)$: $\psi\bar{\psi} \rightarrow \text{anything}$ [44],

$$\frac{d^2}{(dQ^2)^2} \Pi(Q^2) \Big|_{Q^2=0} = -\frac{8}{\pi y^2} \int \frac{dE}{E} \left(1 - \frac{m^2}{E^2}\right)^2 \sigma_{\text{tot}}(E) + O(y^2). \quad (5.5)$$

Here, the integral in the right-hand side converges because the physical cross section is related to the probability and cannot grow fast with energy. Now, recall that the standard perturbation theory reliably calculates the two-point function at low Euclidean momenta, and all nonperturbative corrections are suppressed as $\exp(-\text{const}/\lambda)$. This means that the contributions of the multiparticle intermediate states are also exponentially small, as well as the $\psi\bar{\psi} \rightarrow n$ cross sections $\sigma_n \leq \sigma_{\text{tot}}$ in the right-hand side. We arrive to the conclusion that $F \sim \lambda \ln \sigma_n < 0$ at arbitrary $n \gg 1$ and E , which is hard to avoid. For example, nihilistic approach [41, 43] of dismissing the dispersion relations altogether barely helps: the theory cease to be sane if the sums over the intermediate states diverge.

Fifth and finally, a notable application of our results exploits the saddle-point solutions themselves. With the proper numerical input, we can establish their reliable properties and form the basis for future half-analytic studies. In particular, Refs. [38–40] derived the controversial formula (1.2) for the ‘‘Higgsplosion’’ scenario using a set of assumptions on the semiclassical configurations at $\lambda n \gg 1$. We can confirm one conjecture: at large multiplicities the energy densities of our numerical solutions form relatively narrow spherical shells of width $\Delta r \propto (\lambda n)^0$ that travel inside parametrically large ‘‘interaction’’ regions $r \lesssim O(\lambda n)^{1/2}$, see Sec. 4.1, Fig. 9, and Eq. (4.3). In the linear regions $t \rightarrow +\infty$ our solutions satisfy even simpler scaling $\phi_{\text{cl}} \propto \sqrt{\lambda n}$, see Eq. (4.2). This supports the ‘‘thin-wall’’ approach of Refs. [39, 58].

On the other hand, we observe that the analytic structure of our semiclassical solutions is different from the one assumed in Refs. [38–40]. An important step of the latter calculation is a deformation of the time contour to the lower half-plane, see the dotted (Higgsplosion) line in Fig. 13a. That would be legitimate if the singularities of solutions were not crossed on the way, or if they were the poles and their contributions could be added back to the exponent F . But in fact, all our computed saddle-point configurations have infinite chains of singularities $t_*(\mathbf{x})$, $t'_*(\mathbf{x})$, etc., below the real time axis (at $\text{Re } t > 0$), as is already clear from the simplest solution (2.11) at $E = n = 0$. In Fig. 12b we visualized the analytic structure of

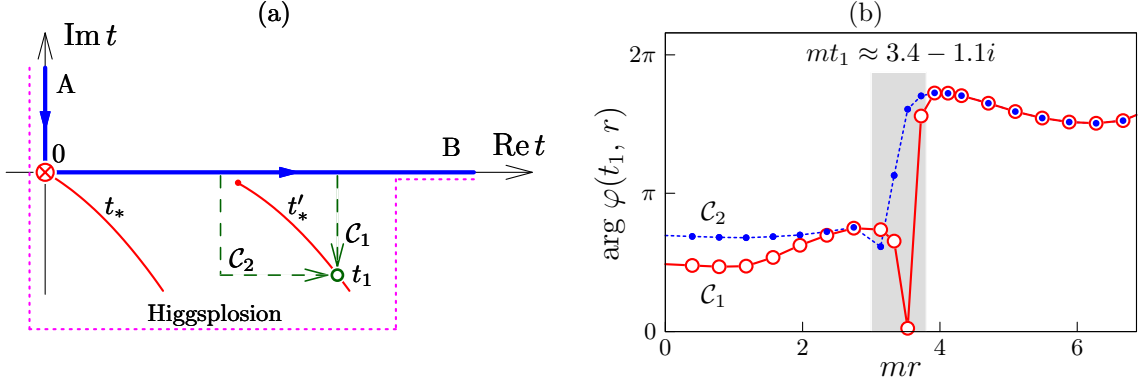


Figure 13: (a) Contours and singularity surfaces in the complex time plane (not to scale). (b) Complex phase of the numerical solution $\phi_{\text{cl}}(t_1, r)$ as a function of r at the point $t = t_1$ of the second chain singularity: $t'_*(r_1) = t_1$. The vicinity of r_1 is indicated by vertical shaded strip. The two graphs (line-points) are obtained using analytic continuations along the contours C_1 and C_2 in Fig. (a). The solution has the following parameters: $\lambda n = 2.51$, $\varepsilon = m/2$, $j_0 = 0.053 m^2$, and $\sigma = 0.29 m^{-1}$.

a particular numerical configuration, see also the movie [66(b)]. Starting from the real time axis where this solution was originally found, we analytically continued it to $\text{Im } t < 0$ and $\text{Im } t > 0$ using the field equation. Then we displayed the complex phase of $\phi_{\text{cl}}(t, 0)$ (color in the figure) and marked the singularities — values of t corresponding to large $|\phi_{\text{cl}}(t, r)|$ at some r — by black solid lines. Three of them are clearly visible in Fig. 12b.

The problem is that these singularities are not poles. In Appendix C we show that the general solution of the field equation (2.1) has the following structure in the vicinity of any singularity:

$$\phi_{\text{cl}} = \frac{C_{-1}(\mathbf{x})}{\tau} + C_0(\mathbf{x}) + C_1(\mathbf{x})\tau + C_2(\mathbf{x})\tau^2 + \left[B(\mathbf{x}) - \frac{1}{5}R_3(\mathbf{x})\ln(m\tau) \right] \tau^3 + \dots \quad (5.6)$$

Here $\tau = it - it'_*(\mathbf{x})$ is the Euclidean time interval to, e.g., the second singularity surface $t'_*(\mathbf{x})$, the functions $t'_*(\mathbf{x})$ and $B(\mathbf{x})$ are the arbitrary Cauchy data, and all other coefficients C_i and R_3 are expressed in their terms via the field equation. Importantly, the last term with $R_3 \neq 0$ includes the logarithm $\ln(m\tau)$ with a branch cut. Moreover, one can show that higher powers of $\ln(m\tau)$ appear in higher orders. This means that the jumps at the branch cuts are nontrivial and the surfaces t_* , t'_* , etc., are the essential singularities. The latter feature is a benchmark property of nonintegrable theories [70] which distinguishes them from exactly solvable cases. We checked it by numerically continuing one of the solutions to the two sides of the branch cut at the singularity point $t = t_1$, where $t'_*(r_1) = t_1$; see the contours C_1 and C_2 in Fig. 13a. Complex phases of the two resulting configurations $\phi_{\text{cl}}(t_1, r)$ are shown by line-points in Fig. 13b, while gray vertical strip marks the region near the singularity $r \approx r_1$. We see that although the two graphs coincide at large r , they are different at $r < r_1$ in compliance with the existing branch cut.

It is worth noting that incorrect choice of the solution branch is very dangerous, as it may give unphysical results for the probability. Thus, it is worth applying our reliable numerical method to the ϕ^4 theory with spontaneously broken symmetry. This will provide a direct test of Eq. (1.2) and give valuable information on the structure of the respective semiclassical solutions.

Recall that our semiclassical solutions with $\varepsilon \gg m$ are not sensitive to the operator $m^2\phi^2$ in the Lagrangian. This suggests that our ultrarelativistic results may be relevant to the spontaneously broken case as well. If this is indeed the case, the multiparticle probability in the broken $\lambda\phi^4$ theory may be given at high ε and large λn by our expression $\mathcal{P}_n \sim \exp\{f_{\infty, \max} n\} \sim \exp\{-2.57 \times n\}$. As the probability grows with energy, we obtain an upper bound $\mathcal{P}_n(\varepsilon) \leq \mathcal{P}_n(\infty)$ at arbitrary ε in the broken case.

From the general perspective, we believe that our numerical approach is scalable and can be used to describe multiparticle processes in other bosonic field theories. It may be even helpful in distinct, but conceptually similar situations, like semiclassical calculations at large U(1) charge [71, 72].

Acknowledgments

This work is supported by the RFBR grant № 20-32-90013. Numerical calculations were performed on the Computational cluster of the Theoretical Division of INR RAS.

A Lattice formulation

Let us describe details of the numerical method. It is convenient to rescale the spherically-symmetric field as $\phi(t, r) = \chi(t, r)/r$. The action (2.13) takes the form,

$$\frac{\lambda S_J}{2\pi} = \int dt \int_0^\infty dr \left[(\partial_t \chi)^2 - (\partial_r \chi)^2 - \chi^2 - \frac{\chi^4}{2r^2} \right] + \int_0^\infty dr \left[2irJ\chi|_{t=0} - \chi\partial_t\chi|_{t_{N_t+1}} \right], \quad (\text{A.1})$$

where $m = 1$, we integrated by parts and ignored boundary terms at $r \rightarrow +\infty$ and $t \rightarrow +i\infty$: the field vanishes exponentially in these regions. We have kept, however, the boundary term at the final time $t = t_{N_t+1}$.

We use uniform spatial lattice. It has $N_r = 256$ sites $r_i \equiv i \cdot \Delta r$ indexed by an integer $0 \leq i \leq N_r - 1$. The sites fill the spherical spatial box of size $R = 6.5 \div 100$. Spacing between them equals $\Delta r = R/(N_r - 1)$. On the other hand, our temporal lattice $\{t_j\}$ is essentially inhomogeneous with steps

$$|\Delta t_j| \equiv |t_{j+1} - t_j| = \Delta t' \left\{ 1 + \alpha \tanh [\beta(j - N_0 - N_1)] - \alpha \tanh [\beta(j - N_0 + N_1)] \right\}, \quad (\text{A.2})$$

where $|\Delta t_j| \approx \Delta t'$ at infinity, the site N_0 corresponds to the moment $t_{N_0} = 0$ when the source acts, and the lattice is denser at $N_0 - N_1 \lesssim j \lesssim N_0 + N_1$ in a way controlled by

the parameters α and β . Recall that t_j cover the complex time contour⁹ A0B in Fig. 3b. Hence, $\Delta t_j = -i|\Delta t_j|$ are purely imaginary at $j < N_0$ and real at larger j . In practice, we choose sufficiently small $\Delta t'$ to resolve the out-waves and make the steps near the source $|\Delta t_{N_0}| = \Delta t' [1 - 2\alpha \tanh(\beta N_1)]$ approximately two orders of magnitude smaller. We specify the region of good resolution with values of N_1 and β and then tune α to the value $\alpha \tanh(\beta N_1) - 1/2 \sim 10^{-2}$. Once the lattice parameters are chosen, we compute the sites t_j and integers N_0, N_t by integrating Eq. (A.2). Our typical lattices have sizes in the range $7061 \leq N_t \leq 12201$, indices $N_0 \sim N_t/3$ of the $t = 0$ site, denser regions with $N_1 \sim N_t/4$, and $\beta^{-1} \sim 10^3$, and deformation coefficients $\alpha \approx 0.57$.

We discretize the action using the field values $\chi_{j,i} = r_i \phi_{j,i}$ at the lattice sites and the second-order finite-difference expressions

$$\partial_t \chi \rightarrow (\chi_{j+1,i} - \chi_{j,i})/\Delta t_j, \quad \partial_r \chi \rightarrow (\chi_{j,i+1} - \chi_{j,i})/\Delta r, \quad \Delta t_j \equiv t_{j+1} - t_j. \quad (\text{A.3})$$

These derivatives are associated with the centers $(j + 1/2, i)$ and $(j, i + 1/2)$ of time and space links, respectively. We also replace the integrals in Eq. (A.1) by the trapezoidal sums. Say,

$$\int dt L(t) \rightarrow \sum_{j=-1}^{N_t} \Delta t_j L_{j+1/2} \quad \text{or} \quad \sum_{j=-1}^{N_t+1} \Delta \bar{t}_j L_j, \quad (\text{A.4})$$

where the first expression is used for the kinetic term $L = (\partial_t \chi)^2$ and the second one — for all the other terms. In Eq. (A.4) we introduced $\Delta \bar{t}_j = (\Delta t_{j-1} + \Delta t_j)/2$ at the inner lattice sites and $\Delta \bar{t}_{-1} = \Delta t_{-1}/2$ and $\Delta \bar{t}_{N_t+1} = \Delta t_{N_t}/2$ at the boundaries. Discretization of the radial integrals is performed in a similar way, but with the uniform spacing Δr , steps $\Delta \bar{r}_i = \Delta r$ at the inner sites, and $\Delta \bar{r}_0 = \Delta \bar{r}_{N_r-1} = \Delta r/2$.

We impose Neumann condition $\partial_r \phi = 0$ at the spatial boundary $r = R$ and require regularity of ϕ at the origin $r = 0$. In terms of $\chi(t, r)$ this reads,

$$\partial_r \chi(t, R) = R^{-1} \chi(t, R) \quad \text{and} \quad \chi(t, 0) = 0. \quad (\text{A.5})$$

To put such conditions on the same footing with the field equation, we add the term $\lambda \Delta S_J / 2\pi = \int dt [\chi^2(t, R)/R - 2\chi(t, 0)\partial_r \chi(t, 0)]$ to the classical action (A.1). After that Eqs. (A.5) are obtained by extremizing S_J with respect to $\chi(t, R)$ and $\chi(t, 0)$. This modification of the action does not change the value of the suppression exponent because the saddle-point value of $\chi_{\text{cl}}(t, R)$ is exponentially small and $\chi_{\text{cl}}(t, 0)$ is zero. We discretize the extra term ΔS_J in the same way as the others.

⁹As we explained in Footnote 3, in certain cases the contour at $j > N_0$ is deformed into the dotted line 0B'B in Fig. 3b. Then the complex phase of Δt_j is determined by the contour tilt.

Substitutions (A.3) and (A.4) give the lattice action,

$$\begin{aligned}
\frac{\lambda S_J}{2\pi} &= \sum_{j=-1}^{N_t} \sum_{i=0}^{N_r-1} \frac{\Delta \bar{r}_i}{\Delta t_j} (\chi_{j+1,i} - \chi_{j,i})^2 - \sum_{j=-1}^{N_t+1} \sum_{i=0}^{N_r-2} \frac{\Delta \bar{t}_j}{\Delta r} (\chi_{j,i+1} - \chi_{j,i})^2 + 2i \sum_{i=0}^{N_r-1} \Delta \bar{r}_i r_i J_i \chi_{N_0,i} \\
&- \sum_{j=-1}^{N_t+1} \sum_{i=0}^{N_r-1} \Delta \bar{t}_j \Delta \bar{r}_i \left(\chi_{j,i}^2 + \frac{\chi_{j,i}^4}{2r_i^2} \right) + \sum_{j=-1}^{N_t+1} \Delta \bar{t}_j \left(\frac{\chi_{j,N_r-1}^2}{R} - \frac{2}{\Delta r} \chi_{j,0} \chi_{j,1} \right) \\
&- \int_0^\infty dr \chi \partial_t \chi \Big|_{t_{N_t+1}}, \tag{A.6}
\end{aligned}$$

where $J_i \equiv J(r_i)$ and the boundary term at $t = t_{N_t+1}$ is still written in the continuous form: we will discretize it later. Lattice field equations and boundary conditions at $r = 0, R$ are obtained by extremizing the first two lines of Eq. (A.6) with respect to $\chi_{j,i}$ at $0 \leq j \leq N_t$ and ignoring the last boundary term; see Eq. (2.14).

Next, we derive finite-difference boundary conditions in the asymptotic past and future. Equation (2.2) can be imposed at the very first time site,

$$\chi_{-1,i} = 0. \tag{A.7}$$

At large positive times, the evolution is linear and the time lattice is almost uniform: $\Delta t_j \approx \Delta t'$. The lattice field equation simplifies,

$$\frac{\chi_{j+1,i} + \chi_{j-1,i} - 2\chi_{j,i}}{\Delta t'^2} - \sum_{i'} \Delta_{i,i'} \chi_{j,i'} + \chi_{j,i} = 0 \quad \text{at large } t_j, \tag{A.8}$$

where the three-diagonal matrix $\Delta_{i,i'}$ replacing the Laplacian can be explicitly deduced from the above action. We solve Eq. (A.8) using the basis of eigenvectors $\psi_i^{(l)}$ diagonalizing the matrix: $\Delta \psi^{(l)} = -k_l^2 \psi^{(l)} \equiv -(\omega_l^2 - 1) \psi^{(l)}$, where k_l are the discrete analogs of momenta and l is an integer. The solution

$$\chi_{j,i} = \sum_{l=1}^{N_r} \frac{\psi_i^{(l)}}{\sqrt{2\omega_l}} \left(a_l e^{-i\mu_l t_j} + b_l^* e^{i\mu_l t_j} \right), \quad \mu_l = \frac{2}{\Delta t'} \arcsin \left\{ \frac{\Delta t'}{2} \omega_l \right\} \tag{A.9}$$

is parametrized by arbitrary complex amplitudes a_l and b_l^* of terms oscillating with lattice frequencies $\pm\mu_l$. In the continuous limit, the eigenvectors turn into spherical harmonics, $\psi_i^{(l)} \propto \sin(k_l r_i)$, the frequencies start to obey the standard dispersion relation $\mu_l^2 \rightarrow k_l^2 + 1$, and a_l and b_l become proportional to the negative- and positive-frequency amplitudes. This discloses Eq. (A.9) as a discrete version of the free wave decomposition (2.3). In practice, we numerically compute the spectrum $\{\psi^{(l)}, k_l^2 \equiv \omega_l^2 - 1\}$ of $\Delta_{i,i'}$ and extract the amplitudes

from the field values at the two last time sites:

$$a_l = \frac{ie^{i\mu_l t_{N_t+1}} \sqrt{\omega_l}}{\sqrt{2} \sin(\mu_l \Delta t')} \sum_{i=0}^{N_r-1} \Delta \bar{r}_i \psi_i^{(l)} \left(\chi_{N_t+1,i} e^{-i\mu_l \Delta t'} - \chi_{N_t,i} \right), \quad (\text{A.10})$$

$$b_l^* = \frac{e^{-i\mu_l t_{N_t+1}} \sqrt{\omega_l}}{i\sqrt{2} \sin(\mu_l \Delta t')} \sum_{i=0}^{N_r-1} \Delta \bar{r}_i \psi_i^{(l)} \left(\chi_{N_t+1,i} e^{i\mu_l \Delta t'} - \chi_{N_t,i} \right),$$

where normalization¹⁰ $\sum_i \Delta \bar{r}_i \psi_i^{(l)} \psi_i^{(l')} = \delta_{ll'}$ is assumed. The final boundary conditions (2.4) in the discrete form¹¹

$$a_l = e^{-\theta+2\omega_l T} b_l \quad (\text{A.11})$$

impose a set of linear relations on $\chi_{N_t,i}$ and $\chi_{N_t+1,i}$.

The last term in the action (A.6) is discretized by replacing

$$\int_0^\infty dr \chi \partial_t \chi \Big|_{t_{N_t+1}} \rightarrow \sum_{i=0}^{N_r-1} \sum_{l=1}^{N_r} \Delta \bar{r}_i \chi_{N_t+1,i} \psi_i^{(l)} \left(\frac{\tilde{\chi}_{N_t+1,l} - \tilde{\chi}_{N_t,l}}{\Delta t_{N_t}} - \frac{\Delta t_{N_t}}{2} \omega_l^2 \tilde{\chi}_{N_t+1,l} \right), \quad (\text{A.12})$$

where $\tilde{\chi}_{j,l} \equiv \sum_i \Delta \bar{r}_i \psi_i^{(l)} \chi_{j,i}$ is the field in the basis of free waves on the lattice. One can check that Eq. (A.12) is the second-order discretization in Δt_j by performing Taylor series expansion in this parameter and using Eq. (A.9).

Given the representation (A.9), we immediately write parameters of the final state as

$$\lambda E = 4\pi \sum_l \omega_l a_l b_l^*, \quad \lambda n = 4\pi \sum_l a_l b_l^*. \quad (\text{A.13})$$

It is straightforward to see that these expressions reproduce Eqs. (2.5) in the continuous limit. In particular, the continuous occupation numbers equal

$$a_{\mathbf{k}} b_{\mathbf{k}}^* \approx \frac{a_l b_l^*}{k_l^2 \Delta k_l}, \quad (\text{A.14})$$

where $\Delta k_l = k_l - k_{l-1} \approx \pi/R$. We exploit this matching to plot Fig. 8.

Discretized field equation (2.14) with the boundary conditions (A.7), (A.11) and expressions (A.13) for λE and λn form an algebraic system of nonlinear equations $G_\alpha = 0$ for the unknowns $y_\alpha \equiv \{\phi_{j,i}, T, \theta\}$. We solve this system as described in the main text. After finding the solution, we compute the suppression exponent F_J using Eqs. (2.7), (A.6), and (A.12).

It is worth noting that the nonlinear energy (2.9) is discretized in the same way as the classical action. We check its conservation along the parts A0 and 0B of the time contour to determine the discretization errors. Also, difference between the exact and free-wave energies, Eqs. (2.9) and (A.13), estimates nonlinear effects in the final state which should be small.

¹⁰This scalar product is related to the fact that the matrix $\Delta \bar{r}_i \Delta_{i,i'}$ is symmetric, while $\Delta_{i,i'}$ itself is not, cf. Eqs. (A.6) and (A.8).

¹¹One eigenvector of $\Delta_{i,i'}$ has the form $\psi_i^{(N_r)} \propto \delta_{0,i}$ due to our choice of the boundary term at $i=0$ in Eq. (A.6). In this case Eq. (A.11) together with the boundary condition $\chi_{j,0} = 0$ ascertain that $a_{N_r} = b_{N_r} \equiv 0$ for all our solutions.

B Solutions in the linear theory

In this Appendix we perform semiclassical calculations in the free theory with a source. Start with the solution (3.1). Evaluating the integral over k^0 in its second term, we get,

$$\phi_{\text{cl}}^{(\text{lin})} = - \int \frac{d^3 \mathbf{k}}{(2\pi)^3} \frac{e^{i\omega_{\mathbf{k}} t - i \mathbf{k} \mathbf{x}}}{2\omega_{\mathbf{k}}} \left[J(-\mathbf{k}) + J^*(\mathbf{k}) e^{\theta - 2\omega_{\mathbf{k}} T} \right] \quad \text{at } t < 0, \quad (\text{B.1})$$

$$\phi_{\text{cl}}^{(\text{lin})} = - \int \frac{d^3 \mathbf{k}}{(2\pi)^3} \frac{e^{i \mathbf{k} \mathbf{x}}}{2\omega_{\mathbf{k}}} \left[J(\mathbf{k}) e^{-i\omega_{\mathbf{k}} t} + J^*(-\mathbf{k}) e^{i\omega_{\mathbf{k}} t + \theta - 2\omega_{\mathbf{k}} T} \right] \quad \text{at } t > 0. \quad (\text{B.2})$$

We analytically continue this function from $t < 0$ to the upper half of imaginary axis $t = i|t|$. Clearly, it decreases as $t \rightarrow +i\infty$ in accordance with Eq. (2.2). At $t > 0$, the configuration (B.2) explicitly satisfies the boundary conditions in the infinite future (2.3), (2.4) with $a_{\mathbf{k}} = -J(\mathbf{k})/\sqrt{2\omega_{\mathbf{k}}(2\pi)^3}$ and $b_{\mathbf{k}} = -J(\mathbf{k}) e^{\theta - 2\omega_{\mathbf{k}} T}/\sqrt{2\omega_{\mathbf{k}}(2\pi)^3}$.

Given $a_{\mathbf{k}}$ and $b_{\mathbf{k}}$, we evaluate the out-state parameters (2.5) as

$$\lambda E = e^{\theta} \int \frac{d^3 \mathbf{k}}{2(2\pi)^3} |J(\mathbf{k})|^2 e^{-2\omega_{\mathbf{k}} T} \quad \lambda n = e^{\theta} \int \frac{d^3 \mathbf{k}}{2\omega_{\mathbf{k}}(2\pi)^3} |J(\mathbf{k})|^2 e^{-2\omega_{\mathbf{k}} T}. \quad (\text{B.3})$$

One can express θ from the second of these equations. Then the first relates T to $\varepsilon = E/n - m$. Finally, the exponent

$$F_J = 2\lambda E T - \lambda n \theta + \text{Re} \int \frac{d^3 \mathbf{k}}{(2\pi)^3} \frac{J(\mathbf{k})}{2\omega_{\mathbf{k}}} \left[J(-\mathbf{k}) + J^*(\mathbf{k}) e^{\theta - 2\omega_{\mathbf{k}} T} \right] \quad (\text{B.4})$$

is obtained by substituting Eq. (3.1) into Eqs. (1.3) and (2.7) and ignoring the interaction term.

We use the above expressions in the following way. For given λn and ε , we express θ and get a nonlinear equation for $T = T(\varepsilon)$ from Eqs. (B.3). The latter equation is solved by binary search [64] and numerical computation of the \mathbf{k} integrals. Recall that we always exploit the Gaussian source (2.12) with the Fourier image

$$J(\mathbf{k}) \equiv \int d^3 \mathbf{x} J(\mathbf{x}) e^{-i \mathbf{k} \mathbf{x}} = j_0 (2\pi\sigma^2)^{3/2} e^{-\mathbf{k}^2 \sigma^2 / 2}. \quad (\text{B.5})$$

We determine the starting configuration for the main numerical procedure of this paper by computing the \mathbf{k} integrals in Eqs. (B.1), (B.2) at every lattice point $(t_j, r_i = |\mathbf{x}|_i)$. The exponent in the linear theory is given by Eq. (B.4). This result for F_J is displayed with the dotted line in Fig. 4a.

C Singularity structure and the limit $J \rightarrow 0$

Let us analyze the structure of semiclassical solutions near their singularities $t = t_*(\mathbf{x})$. This will establish their j_0 dependence and allow us to perform extrapolation $j_0 \rightarrow 0$. Also, we will be able to prove that the ‘‘main’’ singularity surface touches the physical contour at $j_0 = 0$.

We introduce Euclidean time interval to the singularity,

$$\tau = i [t - t_*(\mathbf{x})], \quad (\text{C.1})$$

and change the coordinates in the field equation (2.1) to τ and \mathbf{x} . This gives:

$$- [1 - (\partial_k t_*)^2] \partial_\tau^2 \phi_{\text{cl}} + 2i \partial_k t_* \partial_k \partial_\tau \phi_{\text{cl}} + i \Delta t_* \partial_\tau \phi_{\text{cl}} - \Delta \phi_{\text{cl}} + m^2 \phi_{\text{cl}} + \phi_{\text{cl}}^3 = 0, \quad (\text{C.2})$$

where $k = 1, 2, 3$ indexes spatial coordinates, Δ is the Laplacian, and we so far ignore the source in the right-hand side of Eq. (2.1). In the vicinity of the singularity, it is natural to use the power series in τ :

$$\phi_{\text{cl}}(\tau, \mathbf{x}) = \sum_{n=-1}^{+\infty} C_n(\tau, \mathbf{x}) \tau^n, \quad (\text{C.3})$$

where the first τ^{-1} term is motivated by the solution (2.11). Soon we will see that the coefficients C_n of the above expansion are either τ -independent or depend slowly (logarithmically) on this coordinate.

We substitute Eq. (C.3) into the field equation and solve it order-by-order in τ . The leading order gives $C_{-1} = \sqrt{2 - 2(\partial_k t_*)^2}$, and in the next orders we obtain the following equations

$$(-\partial_\tau^2 + 6\tau^{-2}) (\tau^n C_n) = \tau^{n-2} R_n. \quad (\text{C.4})$$

Here R_n depend on $t_*(\mathbf{x})$ as well as on the coefficients C_m with lower index $m \leq n-1$; one can explicitly deduce these right-hand sides from Eq. (C.2). It is clear that Eq. (C.4) sequentially determines C_n . In particular,

$$C_n = -\frac{R_n[t_*, C_{n-1}, C_{n-2}, \dots]}{(n+2)(n-3)} \quad \text{with} \quad n = 0, 1, \text{ or } 2 \quad (\text{C.5})$$

do not depend on τ . They can be expressed in terms of $t_*(\mathbf{x})$ and its derivatives by substituting all previous C_m with $m \leq n-1$ into R_n .

But there are two subtleties. First, the operator in the left-hand side of Eq. (C.4) annihilates the function

$$\delta \phi_{\text{cl}} = \frac{i C_{-1}}{\tau^2} \delta t_*(\mathbf{x}) + B(\mathbf{x}) \tau^3 \quad (\text{C.6})$$

for arbitrary $\delta t_*(\mathbf{x})$ and $B(\mathbf{x})$. This is the freedom of solving Eqs. (C.4): we can change the singularity surface $t_* \rightarrow t_*(\mathbf{x}) + \delta t_*(\mathbf{x})$ and add τ -independent part $B(\mathbf{x})$ to C_3 . Second, the coefficient C_3 itself cannot be τ -independent, or Eq. (C.4) would not be satisfied at $n = 3$. Indeed, the left-hand side of this equation equals zero for $C_3 = B(\mathbf{x})$ in disagreement with

$$R_3(\mathbf{x}) = \frac{2}{C_{-1}^3} \partial_k (-4i C_{-1} C_2 \partial_k t_* + C_{-1} \partial_k C_1 - C_1 \partial_k C_{-1}) \neq 0. \quad (\text{C.7})$$

In particular, $R_3(0) = 2\sqrt{2} [m \Delta t_*(0)/3]^2 \neq 0$ at $\mathbf{x} = 0$ in the spherically-symmetric case. Solving Eq. (C.4) at $n = 3$, we obtain,

$$C_3(\tau, \mathbf{x}) = B(\mathbf{x}) - \frac{1}{5} R_3(\mathbf{x}) \ln(m\tau), \quad (\text{C.8})$$

where the logarithmic term is important for establishing the analytic structure of the solution. Now, it is clear that the singularity $t = t_*(\mathbf{x})$ is a branching point.

One can demonstrate that at higher orders $n \geq 4$ the coefficients $C_n(\tau, \mathbf{x})$ include powers of $\ln(m\tau)$ coming from nonlinear terms in the right-hand sides R_n . This tells us that $t = t_*(\mathbf{x})$ is an essential singularity with a branch cut. It is worth reminding that existence of such singularities in the general solution is a benchmark property of nonintegrable models like our scalar $\lambda\phi^4$ theory.

To sum up, the recurrent relations (C.4) express all $C_n(\tau, \mathbf{x})$ in terms of two arbitrary functions $t_*(\mathbf{x})$ and $B(\mathbf{x})$. This is the precisely the amount of Cauchy data required for the second-order field equation; hence, general solution of the latter has the form (C.3) near every singularity, indeed. Thereby, we justified Eq. (5.6) from the main text. Representation (C.3) with logarithmically dependent coefficients is known in the literature as logarithmic Ψ series [70].

Now, let us restore the source $J(\mathbf{x})$ at $t = 0$ in the right-hand side of the field equation. The respective solution consists of two analytic functions $\phi_{\text{cl}}^-(t, \mathbf{x})$ and $\phi_{\text{cl}}^+(t, \mathbf{x})$ defined on the intervals A0 and 0B of the complex time contour. The functions are sewed at $t = 0$ according to Eqs. (2.6). Assuming that ϕ_{cl}^\pm have singularities near $t = \mathbf{x} = 0$, we can write them as the series (C.3) in the vicinity of this point. We thus parametrize the two parts of the solution with $t_*^\pm(\mathbf{x})$ and $B^\pm(\mathbf{x})$. To the leading order in t_* , the sewing conditions give,

$$t_*^+ - t_*^- \approx -\frac{J(\mathbf{x}) t_*^3(\mathbf{x})}{5\sqrt{2}}, \quad B^+ - B^- \approx -\frac{J(\mathbf{x})}{5 t_*^2(\mathbf{x})}. \quad (\text{C.9})$$

We see that the difference between the two singularity surfaces $t_*^\pm \approx t_*$ is parametrically suppressed by both $t_*^3(\mathbf{x})$ and $J(\mathbf{x})$, whereas the jump of the parameter B may be large [54]. This justifies Eq. (4.1) which includes a single singularity surface.

Next, we extract j_0 dependence of the solution using the expression (2.10) for energy. Indeed, since the source is narrow, the integral in that expression is saturated in the small vicinity of $t = \mathbf{x} = 0$ where we can adopt the approximation (4.1): use the leading singular term $\phi_{\text{cl}}^\pm \approx \sqrt{2}/\tau$ of the solution and ignore difference between the two singularity surfaces $t_*^\pm(\mathbf{x}) \approx t_{*,0} + t_{*,2} \mathbf{x}^2$. Here the complex parameters $t_{*,0}$ and $t_{*,2} \equiv \Delta t_*(0)/6$ characterize shift and curvature of the singularity surface at $\mathbf{x} = 0$. Expression (2.10) takes the form,

$$\lambda E \approx - \int \frac{J(\mathbf{x}) d^3\mathbf{x} \sqrt{2}}{(t_{*,0} + t_{*,2} \mathbf{x}^2)^2} = \frac{4\pi j_0 \sqrt{2}}{(it_{*,0})^{1/2} (it_{*,2})^{3/2}} \left[\frac{\pi}{4} e^\zeta (1 + 2\zeta) \operatorname{erfc} \sqrt{\zeta} - \frac{\sqrt{\pi\zeta}}{2} \right], \quad (\text{C.10})$$

where in the second equality we calculated the integral for the Gaussian source (2.12) of strength j_0 and width σ . We also introduced a combination $\zeta = t_{*,0}/(2t_{*,2} \sigma^2)$ and exploited the complementary error function $\operatorname{erfc}(z)$.

Suppose the singularity surface remains smooth in the limit $j_0 \rightarrow 0$ and $j_0/\sigma = \text{const}$, i.e. $t_{*,2}$ is finite. Then finiteness of energy E in this limit implies that $t_{*,0} \rightarrow O(j_0^2)$ and ζ

tends to a constant. This result is used in Sec. 4.1 and numerically confirmed¹² in Fig. 7b. It implies, in particular, that the singularity surface touches the point $t = \mathbf{x} = 0$ and the semiclassical solutions are truly singular at $j_0 = 0$. Besides, together with Eqs. (C.9) this scaling establishes sewing condition between the two parts of solutions at zero source [54]: their singularity surfaces should coincide, $t_*^+ = t_*^-$, and the jump of $B(\mathbf{x})$ should be proportional to the δ -function: $B^+ - B^- = \lambda E \delta^3(\mathbf{x})/5\sqrt{2}$. Note that the latter condition should be taken cautiously, as powers of B are present in the higher-order terms of the Ψ series.

We are ready to conclude that the semiclassical solution and all its characteristics F_J , θ , and T can be expressed as power series in j_0^2 at $j_0/\sigma = \text{const}$. Indeed, although relation (C.10) was derived in the leading order, corrections to it go in powers of $t_*(\mathbf{x}) \propto j_0^2$. Thus, the solution $t_{*,0}$ of this equation can be expressed as series in j_0^2 at a fixed energy. Expanding the coefficients in Eq. (C.3) — nonlinear functions of $t_*(\mathbf{x})$ — in corrections, one turns the entire solution into series in j_0^2 . This fact was used in Sec. 3 for extrapolating results to $j_0 = 0$, see Eq. (3.4).

References

- [1] A. Ringwald, *High-Energy Breakdown of Perturbation Theory in the Electroweak Instanton Sector*, *Nucl. Phys. B* **330** (1990) 1.
- [2] O. Espinosa, *High-Energy Behavior of Baryon and Lepton Number Violating Scattering Amplitudes and Breakdown of Unitarity in the Standard Model*, *Nucl. Phys. B* **343** (1990) 310.
- [3] J. M. Cornwall, *On the High-energy Behavior of Weakly Coupled Gauge Theories*, *Phys. Lett. B* **243** (1990) 271.
- [4] H. Goldberg, *Breakdown of perturbation theory at tree level in theories with scalars*, *Phys. Lett. B* **246** (1990) 445.
- [5] L. S. Brown, *Summing tree graphs at threshold*, *Phys. Rev. D* **46** (1992) R4125, [[hep-ph/9209203](#)].
- [6] M. B. Voloshin, *Summing one loop graphs at multiparticle threshold*, *Phys. Rev. D* **47** (1993) R357, [[hep-ph/9209240](#)].
- [7] B. H. Smith, *Summing one loop graphs in a theory with broken symmetry*, *Phys. Rev. D* **47** (1993) 3518, [[hep-ph/9209287](#)].
- [8] M. V. Libanov, V. A. Rubakov, D. T. Son and S. V. Troitsky, *Exponentiation of multiparticle amplitudes in scalar theories*, *Phys. Rev. D* **50** (1994) 7553, [[hep-ph/9407381](#)].
- [9] M. V. Libanov, V. A. Rubakov and S. V. Troitsky, *Multiparticle processes and semiclassical analysis in bosonic field theories*, *Phys. Part. Nucl.* **28** (1997) 217.
- [10] M. Dine, H. H. Patel and J. F. Ulbricht, *Behavior of Cross Sections for Large Numbers of Particles*, [2002.12449](#).

¹²We performed a stronger test. To this end we computed the singularity surfaces of the numerical solutions at different j_0/σ and small j_0 . The combinations $j_0/(t_{*,0}^2 t_{*,2}^3)$ and ζ were related by Eq. (C.10).

- [11] E. N. Argyres, R. H. P. Kleiss and C. G. Papadopoulos, *Amplitude estimates for multi - Higgs production at high-energies*, *Nucl. Phys. B* **391** (1993) 42.
- [12] B. H. Smith, *Properties of perturbative multiparticle amplitudes in ϕ^{**k} and $O(N)$ theories*, *Phys. Rev. D* **47** (1993) 3521, [[hep-ph/9211238](#)].
- [13] M. V. Libanov, V. A. Rubakov and S. V. Troitsky, *Tree amplitudes at multiparticle threshold in a model with softly broken $0(2)$ symmetry*, *Nucl. Phys. B* **412** (1994) 607, [[hep-ph/9307213](#)].
- [14] V. V. Khoze, *Multiparticle Higgs and Vector Boson Amplitudes at Threshold*, *JHEP* **07** (2014) 008, [[1404.4876](#)].
- [15] S. Schenk, *The breakdown of resummed perturbation theory at high energies*, *JHEP* **03** (2022) 100, [[2109.00549](#)].
- [16] V. V. Khoze and S. Schenk, *Multiparticle amplitudes in a scalar EFT*, *JHEP* **05** (2022) 134, [[2203.03654](#)].
- [17] E. N. Argyres, C. G. Papadopoulos and R. H. P. Kleiss, *Multiscalar production amplitudes beyond threshold*, *Nucl. Phys. B* **395** (1993) 3, [[hep-ph/9211237](#)].
- [18] V. V. Khoze, *Perturbative growth of high-multiplicity W , Z and Higgs production processes at high energies*, *JHEP* **03** (2015) 038, [[1411.2925](#)].
- [19] C. Bachas, *A Proof of exponential suppression of high-energy transitions in the anharmonic oscillator*, *Nucl. Phys. B* **377** (1992) 622.
- [20] J. Jaeckel and S. Schenk, *Exploring High Multiplicity Amplitudes in Quantum Mechanics*, *Phys. Rev. D* **98** (2018) 096007, [[1806.01857](#)].
- [21] J. Jaeckel and S. Schenk, *Exploring high multiplicity amplitudes: The quantum mechanics analogue of the spontaneously broken case*, *Phys. Rev. D* **99** (2019) 056010, [[1811.12116](#)].
- [22] M. V. Libanov, D. T. Son and S. V. Troitsky, *Exponentiation of multiparticle amplitudes in scalar theories. 2. Universality of the exponent*, *Phys. Rev. D* **52** (1995) 3679, [[hep-ph/9503412](#)].
- [23] V. A. Rubakov, D. T. Son and P. G. Tinyakov, *Classical boundary value problem for instanton transitions at high-energies*, *Phys. Lett. B* **287** (1992) 342.
- [24] P. G. Tinyakov, *Multiparticle instanton induced processes and B violation in high-energy collisions*, *Phys. Lett. B* **284** (1992) 410.
- [25] A. H. Mueller, *Comparing two particle and multiparticle initiated processes in the one instanton sector*, *Nucl. Phys. B* **401** (1993) 93.
- [26] G. F. Bonini, A. G. Cohen, C. Rebbi and V. A. Rubakov, *The Semiclassical description of tunneling in scattering with multiple degrees of freedom*, *Phys. Rev. D* **60** (1999) 076004, [[hep-ph/9901226](#)].
- [27] D. G. Levkov, A. G. Panin and S. M. Sibiryakov, *Signatures of unstable semiclassical trajectories in tunneling*, *J. Phys. A* **42** (2009) 205102, [[0811.3391](#)].
- [28] V. G. Kiselev, *False vacuum decay induced by a two particle collision in two-dimensions*, *Phys. Rev. D* **45** (1992) 2929.

- [29] V. A. Rubakov, D. T. Son and P. G. Tinyakov, *Initial state independence of nonperturbative scattering through thin wall bubbles in (1+1)-dimensions*, *Phys. Lett. B* **278** (1992) 279.
- [30] A. N. Kuznetsov and P. G. Tinyakov, *False vacuum decay induced by particle collisions*, *Phys. Rev. D* **56** (1997) 1156, [[hep-ph/9703256](#)].
- [31] F. L. Bezrukov, D. Levkov, C. Rebbi, V. A. Rubakov and P. Tinyakov, *Semiclassical study of baryon and lepton number violation in high-energy electroweak collisions*, *Phys. Rev. D* **68** (2003) 036005, [[hep-ph/0304180](#)].
- [32] F. L. Bezrukov, D. Levkov, C. Rebbi, V. A. Rubakov and P. Tinyakov, *Suppression of baryon number violation in electroweak collisions: Numerical results*, *Phys. Lett. B* **574** (2003) 75, [[hep-ph/0305300](#)].
- [33] D. G. Levkov and S. M. Sibiryakov, *Induced tunneling in QFT: Soliton creation in collisions of highly energetic particles*, *Phys. Rev. D* **71** (2005) 025001, [[hep-th/0410198](#)].
- [34] D. Levkov and S. Sibiryakov, *Real-time instantons and suppression of collision-induced tunneling*, *JETP Lett.* **81** (2005) 53, [[hep-th/0412253](#)].
- [35] S. V. Demidov and D. G. Levkov, *Soliton-antisoliton pair production in particle collisions*, *Phys. Rev. Lett.* **107** (2011) 071601, [[1103.0013](#)].
- [36] S. V. Demidov and D. G. Levkov, *Semiclassical description of soliton-antisoliton pair production in particle collisions*, *JHEP* **11** (2015) 066, [[1509.07125](#)].
- [37] S. Demidov and D. Levkov, *High-energy limit of collision-induced false vacuum decay*, *JHEP* **06** (2015) 123, [[1503.06339](#)].
- [38] V. V. Khoze and M. Spannowsky, *Higgspllosion: Solving the hierarchy problem via rapid decays of heavy states into multiple Higgs bosons*, *Nucl. Phys. B* **926** (2018) 95, [[1704.03447](#)].
- [39] V. V. Khoze, *Multiparticle production in the large λn limit: realising Higgspllosion in a scalar QFT*, *JHEP* **06** (2017) 148, [[1705.04365](#)].
- [40] V. V. Khoze and J. Reiness, *Review of the semiclassical formalism for multiparticle production at high energies*, *Phys. Rept.* **822** (2019) 1, [[1810.01722](#)].
- [41] A. Belyaev, F. Bezrukov, C. Shepherd and D. Ross, *Problems with Higgspllosion*, *Phys. Rev. D* **98** (2018) 113001, [[1808.05641](#)].
- [42] A. Monin, *Inconsistencies of Higgspllosion*, [1808.05810](#).
- [43] V. V. Khoze and M. Spannowsky, *Consistency of Higgspllosion in Localizable QFT*, *Phys. Lett. B* **790** (2019) 466, [[1809.11141](#)].
- [44] V. I. Zakharov, *High-energy production of scalar bosons in weak coupling theories*, *Phys. Rev. Lett.* **67** (1991) 3650.
- [45] G. Veneziano, *Bound on reliable one-instanton cross-sections*, *Mod. Phys. Lett. A* **7** (1992) 1661.
- [46] M. Maggiore and M. A. Shifman, *Nonperturbative processes at high energies in weakly coupled theories: Multi-instantons set an early limit*, *Nucl. Phys. B* **371** (1992) 177.
- [47] V. V. Khoze and M. Spannowsky, *Higgsploding universe*, *Phys. Rev. D* **96** (2017) 075042, [[1707.01531](#)].

- [48] M. B. Voloshin, *Loops with heavy particles in production amplitudes for multiple Higgs bosons*, *Phys. Rev. D* **95** (2017) 113003, [[1704.07320](#)].
- [49] V. A. Rubakov, *Nonperturbative aspects of multiparticle production*, in *2nd Rencontres du Vietnam*, 10, 1995, [hep-ph/9511236](#).
- [50] C. Rebbi and R. L. Singleton, Jr, *Computational study of baryon number violation in high-energy electroweak collisions*, *Phys. Rev. D* **54** (1996) 1020, [[hep-ph/9601260](#)].
- [51] S. V. Demidov and D. G. Levkov, *Soliton pair creation in classical wave scattering*, *JHEP* **06** (2011) 016, [[1103.2133](#)].
- [52] S. V. Demidov and B. R. Farkhtdinov, *Numerical study of multiparticle scattering in $\lambda\phi^4$ theory*, *JHEP* **11** (2018) 068, [[1806.10996](#)].
- [53] S. V. Demidov, B. R. Farkhtdinov and D. G. Levkov, *Numerical Study of Multiparticle Production in ϕ^4 Theory: Comparison with Analytical Results*, *JETP Lett.* **114** (2021) 649, [[2111.04760](#)].
- [54] D. T. Son, *Semiclassical approach for multiparticle production in scalar theories*, *Nucl. Phys. B* **477** (1996) 378, [[hep-ph/9505338](#)].
- [55] L. D. Landau and E. M. Lifshits, *Quantum Mechanics: Non-Relativistic Theory*, vol. 3 of *Course of Theoretical Physics*. Butterworth-Heinemann, Oxford, 1991.
- [56] M. B. Voloshin, *Strong high-energy scattering in theories with weak coupling*, *Phys. Rev. D* **43** (1991) 1726.
- [57] S. Y. Khlebnikov, *Semiclassical approach to multiparticle production*, *Phys. Lett. B* **282** (1992) 459.
- [58] A. S. Gorsky and M. B. Voloshin, *Nonperturbative production of multiboson states and quantum bubbles*, *Phys. Rev. D* **48** (1993) 3843, [[hep-ph/9305219](#)].
- [59] D. Diakonov and V. Petrov, *Nonperturbative isotropic multiparticle production in Yang-Mills theory*, *Phys. Rev. D* **50** (1994) 266, [[hep-ph/9307356](#)].
- [60] P. G. Tinyakov, *Instanton like transitions in high-energy collisions*, *Int. J. Mod. Phys. A* **8** (1993) 1823.
- [61] F. L. Bezrukov, *Use of singular classical solutions for calculation of multiparticle cross-sections in field theory*, *Theor. Math. Phys.* **115** (1998) 647, [[hep-ph/9901270](#)].
- [62] F. L. Bezrukov, M. V. Libanov and S. V. Troitsky, *$O(4)$ symmetric singular solutions and multiparticle cross-sections in ϕ^{**4} theory at tree level*, *Mod. Phys. Lett. A* **10** (1995) 2135, [[hep-ph/9508220](#)].
- [63] Ancillary files: “[info.pdf](#)” describes published data, “[finite_J.dat](#)” provides numerical results at finite source $J(\boldsymbol{x})$, “[zero_J.dat](#)” — results of extrapolation to $J = 0$, “[large_n.dat](#)” — functions $f_\infty(\varepsilon)$, $g_\infty(\varepsilon)$, and $f(\varepsilon)$, “[solution.mp4](#)”, “[solution.white.mp4](#)”, and “[video_poles.mp4](#)” — the movies [[66](#)].
- [64] W. Press, S. Teukolsky, W. Vetterling and B. Flannery, *Numerical Recipes: The Art of Scientific Computing*. Cambridge University Press, 3 ed., 2007.
- [65] NVIDIA, P. Vingelmann and F. H. Fitzek, “[Cuda, release: 10.2.89.](#)” <https://developer.nvidia.com/cuda-toolkit>, 2020.

- [66] Movies showing (a) the semiclassical solution $\phi_{c1}(t, r)$ from Fig. 5 as a function of x and y at $z = 0$ evolving with time t ; (b) the solution from Fig. 12b plotted with color in the complex time plane at different r . See https://www.youtube.com/playlist?list=PLwjyEqTkiXRL78rd-UjGt_kv-jyS7iqPt, 2022.
- [67] M. Froissart, *Asymptotic behavior and subtractions in the Mandelstam representation*, *Phys. Rev.* **123** (1961) 1053.
- [68] L. D. Landau and E. M. Lifshitz, *Statistical Physics, Part 1*, vol. 5 of *Course of Theoretical Physics*. Butterworth-Heinemann, Oxford, 1980.
- [69] J. M. Cornwall and G. Tiktopoulos, *Semiclassical matrix elements for the quartic oscillator*, *Annals Phys.* **228** (1993) 365.
- [70] M. Tabor, *Chaos and integrability in nonlinear dynamics : an introduction*. New York (N.Y.) : Wiley, 1989.
- [71] D. Levkov, E. Nugaev and A. Popescu, *The fate of small classically stable Q-balls*, *JHEP* **12** (2017) 131, [[1711.05279](#)].
- [72] G. Badel, G. Cuomo, A. Monin and R. Rattazzi, *The Epsilon Expansion Meets Semiclassics*, *JHEP* **11** (2019) 110, [[1909.01269](#)].